Monthly Notices of the ROYAL ASTRONOMICAL SOCIETY
MNRAS **457,** 704–722 (2016) doi:10.1093/mnras/stv3004

The long-term *Swift* observations of the high-energy peaked BL Lacertae source 1ES 1959+650

B. Kapanadze,[1,2,3★] P. Romano,[2] S. Vercellone,[2] S. Kapanadze,[1] T. Mdzinarishvili[1] and G. Kharshiladze[4]

[1]*E. Kharadze Abastumani Astrophysical Observatory, Ilia State University, Colokashvili Av. 3/5, Tbilisi, Georgia, 0162*
[2]*INAF, Istituto di Astrofisica Spaziale e Fisica Cosmica, Via U. La Malfa 153, I-90146 Palermo, Italy*
[3]*Astronomy Department, University of Michigan, Ann Arbor, MI 48109-1107, USA (Guest Scientist)*
[4]*Georgian Technical University, Kostava 77, Tbilisi, Georgia, 0175*

Accepted 2015 December 22. Received 2015 December 21; in original form 2015 August 3

ABSTRACT

We present the results based on the monitoring of the high-energy peaked BL Lacertae object 1ES 1959+650 by the *Swift* satellite during 2005–2014. Our timing study shows that the source was highly variable on longer (weeks-to-months) time-scales with the 0.3–10 keV fluxes ranging by a factor of 8. It sometimes showed a significant intra-day variability in the course of ∼1 ks, detected mainly in the epochs of higher brightness states. The flux variability exhibited an erratic character and no signatures of periodic variations are revealed. The X-ray spectra were mainly curved with broad ranges of photon index, curvature parameter, hardness ratio, synchrotron spectral energy distribution (SED) peak location which exhibited a significant variability with the flux at different time-scales. Our study of multi-wavelength cross-correlations shows that the one-zone synchrotron self-Compton scenario was not always valid for 1ES 1959+650. The X-ray flares were sometimes not accompanied with an increasing activity in the γ-ray or lower-energy parts of the spectrum and vice versa. Similar to the prominent 'orphan' TeV event in 2002, significant flares in the high-energy and very high energy bands in 2009 May and 2012 May were not accompanied by those in the synchrotron part of the spectrum. Similar to other TeV-detected high-energy peaked BLLs, the stochastic acceleration of the electrons from the magnetic turbulence close to the shock front may be more important for our target compared to other scenarios since it showed mainly broader synchrotron SEDs during the X-ray flares expected when the stochastic mechanism is more efficient.

Key words: BL Lacertae objects: individual: 1ES 1959+650.

1 INTRODUCTION

BL Lacertae objects (BLLs) are widely accepted to be active galactic nuclei (AGNs) with a relativistic jet closely aligned with the line of sight. This interpretation is successfully explaining their prominent features like compact and flat-spectrum radio emission, superluminal motion, non-thermal continuum emission across the whole spectrum, an almost featureless optical spectrum and significant flux variability in all spectral bands. Their spectral energy distribution (SED) shows the presence of two well-defined broad components in the log νF_ν–log ν representation. The lower-frequency component is explained by synchrotron radiation emitted by relativistic electrons in the jet, while an inverse Compton (IC) scattering of synchrotron photons by the same electron population is thought to be a source for the high-frequency bump (Celotti & Ghisellini 2008).

In this paper, we report the results from the monitoring of high-energy peaked BLL (HBL) source (i.e. a BLL with a synchrotron component peaking in at the UV–X-ray frequencies; Padovani & Giommi 1995) 1ES 1959+650, performed by the *Swift* satellite (Gehrels et al. 2004) during 2005–2013. It was originally detected by Elvis et al. (1992) using the 'Slew Survey' observations performed by *Einstein Observatory* (*HEAO 2*; Giacconi et al. 1979) during 1980–1981. The X-ray source was optically identified as a BLL by Schachter et al. (1993) situated at the redshift $z = 0.047$. Later, the redshift value was adjusted to $z = 0.048$ using the higher-quality spectra (Perlman et al. 1996), and the *Hubble Space Telescope* observation showed the presence of a bright elliptical host galaxy (Scarpa et al. 2000). The TeV-detection of 1ES 1959+650 (Nishiyama 1999) triggered different multi-wavelength campaigns which

★E-mail: bidzina_kapanadze@iliauni.edu.ge

revealed its strong variability in different spectral bands. Namely, Giebels et al. (2002) reported the presence of three successive X-ray flares by a factor up to 3 from the observations performed by the Proportional Counter Array (PCA) onboard the *Rossi X-Ray Timing Explorer (RXTE)* and the *Advanced Research and Global Observation Satellite (ARGOS)* in the 1–16 keV energy band during 2000 July–November, accompanied by a significant spectral variability. Tagliaferri et al. (2003) found the source in the high X-ray state in the case of the two *BeppoSAX* pointings of 2011 September 25–29 corresponding to the 2–10 keV flux $F_{2-10\,\mathrm{keV}} = (0.83 - 1.06) \times 10^{-10}$ erg cm^{-2} s^{-1}. During the three *XMM–Newton* observations of 2002 November to 2003 February, the 2–10 keV flux varied in the range of (6.9–29.6) $\times$ 10^{-11} erg cm^{-2} s^{-1} (Perlman et al. 2005). Krawczynski et al. (2004) revealed several strong flares from the contemporaneous observations of Whipple, HEGRA and *RXTE*-PCA. Although the X-ray and γ-ray fluxes were correlated in general, an 'orphan' gamma-ray flare, not being accompanied by an increasing activity in other spectral bands, was also detected. The 10 keV flux decreased by a factor of 18 in 28 d. In 2003 April–May, the source showed an increased level of X-ray activity – the 10 keV flux varied by a factor of 3.4 (the *RXTE*-PCA observations). However, the Whipple campaign did not reveal any TeV flare (Gutierrez et al. 2006). Albert et al. (2006) reported the detection of a very high energy (VHE; $E > 100$ GeV) emission during the MAGIC 2004 September–October observations at the time of a low activity in both the optical and X-ray bands. Tagliaferri et al. (2008, hereafter T08) found 1ES 1959+650 in one of the lowest historical VHE states during the 2006 May multi-wavelength campaign while the source exhibited a relatively high state in X-ray and optical bands. The simultaneous VERITAS, *Fermi*-LAT and *RXTE*-PCA observations of 2007–2011 revealed the X-ray flux to vary by an order of magnitude, while other energy regimes exhibited less variable emission (Aliu et al. 2013). The source showed four consecutive long-term flares in the *R* band of the Johnson–Cousins system with flux increases by a factor of 1.5–2 during the 2002–2007 observations with the 70 cm Meniscus Telescope of Abastumani Observatory (Georgia; Kapanadze & Janiashvili 2012). It exhibited a long-term optical variability by 0.85–1.23 mag in the *B, V, R, I* bands of the same system, respectively, from the 2009 July–2010 November observations performed with the 50 cm to 2 m telescopes of different observatories (Gaur et al. 2012). Sorcia et al. (2013) reported a long-term optical *R*-band flux variability by 1.12 mag during 2007 October 18 to 2011 May 5. The source underwent a fast VHE variability within 1.5 h during the VERITAS observation of 2012 May – an increase and decay by 70 and 80 per cent of the Crab nebula, respectively (Aliu et al. 2014).

First of all, we concentrate on the 0.3–10 keV band observations performed by the X-ray Telescope (XRT; Burrows et al. 2005), since, according to the basic scenario, the X-ray emission is due to a synchrotron radiation from the highest-energy electrons, and, therefore, a complex spectral variability observed in this band reflects the injection and radiative evolution of freshly accelerated particles (Chiappetti et al. 1999). Thanks to the unique characteristics, good photon statistics and the low background counts of this instrument, we are able to search for a flux variability at different time-scales from minutes to years, to obtain high-quality spectra for the majority of the observations, to derive different spectral parameters and to study their timing behaviour. Along with these data, we have analysed the observations performed with the Ultraviolet-Optical Telescope (UVOT; Roming et al. 2005) and the Burst Alert Telescope (BAT; Barthelmy et al. 2005) onboard the *Swift* satellite. We also constructed the light curves for the same 2005–2013 period using the publicly available VHE (MAGIC, VERITAS), high energy (HE; $E > 1$ MeV, *Fermi*-LAT), optical (*R* band, different Earth-based telescopes), radio (the OVRO 40-m telescope; Richards et al. 2011) observations to draw conclusions about the target's long-term multi-wavelength behaviour and to search for the inter-band correlations.

The paper is organized as follows. Section 2 describes the data processing and analysing procedures. In Section 3, we provide the results of a timing analysis and those from the X-ray spectroscopy in Section 4. The inter-band correlations are presented in Section 5. We discuss our results in Section 6 and provide our conclusions in Section 7.

2 OBSERVATIONS AND DATA REDUCTION

2.1 X-ray data

We retrieved the XRT data from publicly available archive, maintained by HEASARC.[1] The Level 1 unscreened event files were processed with the XRTDAS package version 2.5.1 developed at the ASI Science Data Center (ASDC) and distributed by HEASARC within the HEASOFT package (v. 6.12). They were reduced, calibrated and cleaned by means of the XRTPIPELINE script (version 0.12.6) using the standard filtering criteria and the latest calibration files of *Swift* CALDB 4.1.3. We selected the events with the 0–2 grades for the Windowed Timing (WT) mode, whereas the range of 0–12 was used for the Photon Counting (PC) observations.

The source and background light curves were extracted with XSELECT. Due to a photon pile-up in the core of the point spread function (PSF) for the fluxes $\gtrsim$0.5 count s^{-1} in the PC mode (see Vaughan et al. 2006, and references therein), the source events were extracted from an annular region with the inner radius ranging from 3 to 8 pixels and an outer radius of 20–40 pixels, depending on the source brightness. The size of a piled-up area was determined by comparing the observed PSF profile with the analytical model developed by Moretti et al. (2005). The source light curve was then corrected using the XRTLCCORR task for the resultant loss of effective area, bad/hot pixels, pile-up, and vignetting. The background counts were extracted from the concentric area, centred on the source, with inner and outer radii of 80 and 120 pixels, respectively. No pile-up corrections were necessary for our targets in the case of the WT observations since their fluxes are generally much less than 100 count s^{-1} above which the correction is necessary (Romano et al. 2006). The background-subtracted and binned light curves were created via the LCURVE task. Generally, we used the 1-min binning for this purpose that always ensured a minimum of 20 count per bin (necessary to use the χ^2-statistics). For some observations, however, we used the larger bins (90–300 s) when the value of reduced chi-square was close to the threshold necessary for the detection of an intra-day flux variability at the 99.9 per cent confidence level in the case of 1 min binning.

We extracted events for the spectral analysis with XSELECT in the same regions used for a light curve generation. The ancillary response files (ARFs) were generated using the XRTMKARF task, with the corrections applied to account for the PSF losses, different extraction regions, vignetting, CCD defects. The latest response matrix from the XRT calibration files has been used. The instrumental channels were combined to include at least 20 photons per bin using

[1] http://heasarc.gsfc.nasa.gov/docs/archive.html

the GRPPHA task. After selecting the best-fitting model for the fixed hydrogen absorption column density $N_{\rm H}$ and derivation of the values of corresponding spectral parameters (see Section 4 for details), we calculated the observed 0.3–2 keV, 2–20 keV and 0.3–10 keV model flux values (in units of erg cm^{-2} s^{-1}) and their errors using the FLUX task. Finally, we derived the unabsorbed fluxes and their errors by means of the convolution of the cflux model with the original absorbed one, performed via the EDITMOD task (see details in Xspec Users' Guide for version 12.9.0.[2])

The BAT data, taken from the *Swift*–BAT 70-Month Hard X-ray Survey catalogue[3] (Baumgartner et al. 2013), have been re-binned using the tool REBINGAUSSLC from the HEASOFT package using the weekly bins. Since these data extend to 2010 August, we used those from the *Swift*–BAT Hard X-ray Transient Monitor programme[4] (Krim et al. 2013) for the 2010 August–2014 October period, re-binned similar to the aforementioned data. However, the source detection was mostly below the 5σ significance (the threshold generally accepted for coded-mask devices; see e.g. Baumgartner et al. 2013) even for a weekly binning and, hence, these data were unsuitable for our study.

2.2 Optical and UV data

The UVOT observations were performed in the photometric bands *V*, *B*, *U*, *UVW1*, *UVM2*, and *UVW2* simultaneously with those of the XRT. The sky-corrected images were retrieved from the *Swift* data archive. The photometry was performed using the standard UVOT software developed and distributed within HEASOFT and the calibration files included in the CALDB. The UVOTSOURCE tool was used to extract the source and background counts, correct for coincidence losses, apply background subtraction, calculate the corresponding magnitude and error. The measurements were performed using the 5 arcsec radius source aperture for *V, B, U* bands, and the 10 arcsec radius for *UVW1*, *UVM2*, *UVW2* bands to take properly into account wider PSFs. The magnitudes were then corrected for the Galactic absorption applying $E(B-V) = 0.146$ mag, derived using the relation (Güver & Özel 2009)

$$N_{\rm H}({\rm cm}^{-2}) = (6.87 \pm 0.27) \times 10^{21} E(B-V), \quad (1)$$

and the $A_\lambda/E(B-V)$ values, calculated using the interstellar extinction curves provided in Fitzpatrick & Massa (2007). The effective wavelength of each UVOT filters was taken from Poole et al. (2008). We converted them into linear fluxes (in mJys) adopting the latest photometric zero-points for each band provided in Breeveld et al. (2011).

2.3 High-energy γ-ray data

We extracted the 300 MeV to 100 GeV fluxes from the 2 weeks binned LAT observations (to warrant the source's detection above the 3σ threshold), available since 2008 August 5. The events of diffuse class (those having the highest probability of being a photon) are extracted from a region of interest (ROI) of radius 10°, centred on the coordinates of 1ES 1959+650, and processed with the *Fermi* SCIENCE TOOLS package (version v10r0p5) with P8R2_V6 instrument response function. A cut on the zenith angle (>100 deg) was applied to reduce contamination from the Earth-albedo γ-rays. The data taken when the rocking angle of the spacecraft is greater than 52° are discarded to avoid contamination from photons from the Earth's limb.

A background model including all γ-ray sources from the *Fermi*-LAT 4-year Point Source Catalogue (3FGL; Acero et al. 2015) within 20° of 1ES 1959+650 is created. The remaining excesses in the ROI are modelled as point sources with a simple power-law spectrum. The spectral parameters of sources within the ROI are left free during the minimization process while those outside of this range were held fixed to the 3FGL catalogue values. A log-parabolic function was used for nearby sources with significant spectral curvature and a power law for those sources without it. The Galactic and extragalactic diffuse γ-ray emission as well as the residual instrumental background is included using the recommended model files GLL_IEM_V06.FITS and ISO_P8R2_SOURCE_V6_V06.TXT. The normalizations of both components in the background model were allowed to vary freely during the spectral fitting.

The photon flux, spectral parameters and test-statistics (TS) for the source are computed using an unbinned likelihood analysis method GTLIKE. Its detection significance σ was then calculated as $\sigma \approx ({\rm TS})^{1/2}$ (Abdo et al. 2009). For the spectral modelling of 1ES 1959+650, we adopted a simple power law, as done in the 3FGL catalogue. In some cases, the spectrum was described well by the log-parabola model, although the spectral curvature was not high ($b < 0.2$). In a few cases, the source was not detectable at the 3σ significance from the 2 weeks binned data, and we calculated the upper limit to the photon flux using the CALCUPPER tool included in the user-contributed package LATANALYSISSCRIPTS (version 0.2.1).[5]

Throughout this paper, the errors are quoted at the 90 per cent confidence level for the one parameter of interest $\Delta_{\chi^2} = 2.71$, unless otherwise stated.

3 TIMING ANALYSIS

3.1 Long-term behaviour

The source was observed by the XRT 117 times between 2005 April 19 and 2014 September 22 with a total exposure time of 171 ks. This monitoring includes our Target of Opportunity observations of 1ES 1959+650 performed during 2014 July 30 and August 11 with a medium urgency.[6] The information about each pointing and the measurement results are provided in Table 1.[7] The results of the UVOT observations are presented in Table 2 where the de-reddened magnitudes and corresponding fluxes are provided for each band. The error related to the corrected flux value (F_0) was calculated via multiplying that of the observed one ($F_{\rm obs}$; derived with the UVOTSOURCE tool) by the factor k defined as $k = F_0/F_{\rm obs} = 10^{0.4A_\lambda}$ where A_λ is the reddening in the given band.

Fig. 1(a) presents the historical light curve from the XRT observations. The 0.3–10 keV flux was highly variable by a factor of 8, and showed several flares which are discussed in detail below. During the 9.5 yr period, the highest and weighted mean fluxes were 13.74 count s^{-1} and 5.92 count s^{-1}, respectively. Therefore, this source is one of the brightest blazars in the X-rays. Fig. 1(b) shows

[2] http://heasarc.gsfc.nasa.gov/docs/software/lheasoft/xanadu//xspec/XspecManual.pdf
[3] http://swift.gsfc.nasa.gov/results/bs70mon/
[4] http://swift.gsfc.nasa.gov/results/transients/
[5] See http://fermi.gsfc.nasa.gov/ssc/data/analysis/scitools//LATAnalysisScripts.html
[6] See https://www.swift.psu.edu/secure/toop/summary.php
[7] The printed version of the paper presents the extracts from Tables 1, 2, 5, 6, 9 and Figs 2, 5, 9, 10. Their full versions are available online.

Table 1. Extract from the summary of the *Swift*–XRT observations. The columns are as follows: (1) – observation ID; (2) and (3) – observation beginning and end, respectively (in UTC); (4) – exposure time (in seconds); (5) – observation mode; (6), (7), and (8) – mean value of the observed flux with its error (in count s^{-1}), reduced χ^2 with corresponding d.o.f., existence of a variability during the observation (V stands for a variability detection; PV for possibly variable; and NV for non-variable), respectively.

Obs ID (1)	Start time (2)	End time (3)	Exp.(s) (4)	Mode (5)	Mean flux (6)	χ^2/d.o.f. (7)	Var. (8)
00035025017	2008-10-05 03:29:00	2008-10-05 10:08:48	3562	PC	6.86(0.17)	1.168/57	NV
00035025018	2008-10-13 00:50:15	2008-10-13 02:33:15	1935	PC	7.96(0.18)	1.345/14	NV
00035025019	2008-10-15 21:48:00	2008-10-15 23:35:14	990	PC	5.62(0.16)	0.551/15	NV
00035025020	2008-10-16 01:22:01	2008-10-16 04:44:48	1147	PC, WT	5.27(0.11)	0.158/15	NV
00035025021	2008-10-18 07:46:00	2008-10-18 09:35:44	1017	PC, WT	6.00(0.12)	0.158/15	NV

Table 2. Extract from the results of the *Swift*–UVOT observations. The flux values in each band are given in units of mJy.

	V		*B*		*U*		*UVW1*		*UVM2*		*UVW2*	
Obs Id	Mag.	Flux	Mag.	Flux	Mag.	Flux	Mag.	Flux	Mag.	Flux	Mag.	Flux
35025001	14.49(0.07)	5.86(0.38)	15.09(0.08)	3.73(0.26)	14.09(0.05)	3.34(0.16)	14.17(0.06)	1.92(0.10)	13.85(0.06)	2.21(0.11)	13.86(0.05)	2.11(0.10)
35025002	14.46(0.04)	6.03(0.20)	14.85 0.03)	4.66(0.10)	14.01(0.04)	3.60(0.08)	13.88(0.04)	2.51(0.07)	13.64(0.04)	2.68(0.07)	13.73(0.04)	2.38(0.07)
35025003	14.40(0.05)	6.37(0.26)	14.79(0.04)	4.92(0.14)	13.91(0.04)	3.94(0.12)	13.78(0.04)	2.75(0.10)	13.60(0.05)	2.78(0.11)	13.69(0.04)	2.47(0.10)
35025004	14.45(0.04)	6.08(0.21)	14.86(0.04)	4.61(0.12)	14.01(0.04)	3.60(0.10)	13.88(0.04)	2.51(0.10)	13.61(0.04)	2.75(0.07)	13.70(0.04)	2.44(0.07)
35025005	14.42(0.06)	6.25(0.33)	14.87(0.05)	4.57(0.19)	13.91(0.04)	3.94(0.16)	13.79(0.07)	2.73(0.12)	13.58(0.06)	2.83(0.14)	13.67(0.05)	2.51(0.10)

the light curves from the UVOT *UVW2* and *B* bands,[8] corrected for the Galactic absorption. They show flares in the epochs of those in the 0.3–10 keV band, although their ranges are smaller – $F_{\rm max}/F_{\rm min}$ is equal to 5.74 and 3.66 for the *UVW2* and *V* bands, respectively. We have also plotted a densely sampled (680 data points) *R*-band light curve from the 2005–2011 period in Fig. 1(c). The data were collected from Kapanadze & Janiashvili (2012), T08, Sorcia et al. (2013), Backes (2011) and Aliu et al. (2014). Since Sorcia et al. (2013) provided their results in mJys, we converted them into magnitudes and corrected for the Galactic absorption. In addition, we subtracted 0.08 mag from the obtained values to make comparable with the data from Kapanadze & Janiashvili (2012), obtained with different aperture radius. From the constructed light curve we observe the four consecutive long-term flares lasting from several months to ∼1 yr and variability amplitudes $A \sim 0.5$–1.0 mag. Fig. 1(d) presents the 15 GHz light curve constructed via the fluxes obtained from the OVRO observations performed since 2008 January 8.[9] The source exhibited a long-term variability with $F_{\rm max}/F_{\rm min} = 2.99$. As for the LAT light curve (Fig. 1e), we do not observe long-term trends lasting longer than two months, and $F_{\rm max}/F_{\rm min} \approx 10.3$ for the 2008 August–2014 September period. The source sometimes showed strong shorter-term flares by a factor of 3–4, reaching the highest 0.3–100 GeV flux value of $(7.76 \pm 0.81) \times 10^{-8}$ ph cm^{-2} s^{-1} in the first half of 2014 January. Finally, Fig. 1(f) presents the VHE light curve from the MAGIC and VERITAS observations, provided by T08, Backes (2011), Aliu et al. (2013, 2014), Uellenbeck (2013), and Furniss (2013). The observations were performed for some restricted periods which revealed the source to be very variable also in this band with two strong outbursts by a factor of 4–9.

Below, we concentrate on the results from the different periods of the *Swift* monitoring, the summary of which for the XRT and UVOT observations is presented in Table 3. For each flux variability event, the corresponding fractional root mean square (rms) variability amplitude and its error are calculated as (Vaughan et al. 2003)

$$F_{\rm var} = 100\left\{\frac{S^2 - \overline{\sigma_{\rm err}^2}}{\overline{F}}\right\}^{1/2} \quad \text{per cent},$$

$$\mathrm{err}(F_{\rm var}) = \left\{\left(\sqrt{\frac{1}{2N}}\frac{\overline{\sigma_{\rm err}^2}}{\overline{x}^2 F_{\rm var}}\right)^2 + \left(\sqrt{\frac{\overline{\sigma_{\rm err}^2}}{N}}\frac{1}{\overline{x}}\right)^2\right\}^{1/2}, \qquad (2)$$

with S^2 the sample variance; $\overline{\sigma_{\rm err}^2}$ the mean square error; and $\overline{F}$ the mean flux.

The multi-wavelength light curves from each period are provided in Fig. 3.

3.2 The 2006–2009 observations

The source showed its highest historical 0.3–10 keV flux during Period 1[10](see Table 3), accompanied by high optical–UV states, although they exhibit a delay with respect to the X-ray one – the *UVW2* and *R*-band fluxes reached their peaks in 2 d and 5 d, respectively, after the X-ray maximum (upper and middle panels of Fig. 2a). A correlated optical–UV–X-ray variability is evident also at the end of Period 2 (Fig. 2b). A high level of the 0.3–10 keV flux was recorded in Period 3 (see Table 3), after which it decayed by a factor of 2.5 in 17 d (Fig. 2c, upper panel). While the *UVW2* and *U*-band fluxes do not show a significant shift on daily time-scales, the *R*-band light curve is lagged by about 9 d with respect to the X-ray one (second panel).

The source exhibited a high multi-wavelength brightness state accompanied by short-term flares during the almost three months in Period 4, although the *R*-band light curve shows a significant

[8] Since the fluxes of 1ES 1959+650 from UVOT bands were highly correlated, the corresponding light curves are similar to each other. Therefore, we present only those from one UV and one optical bands.

[9] http://www.astro.caltech.edu/ovroblazars/data/

[10] See T08 for a detailed description of the multi-wavelength campaign performed in 2006 May.

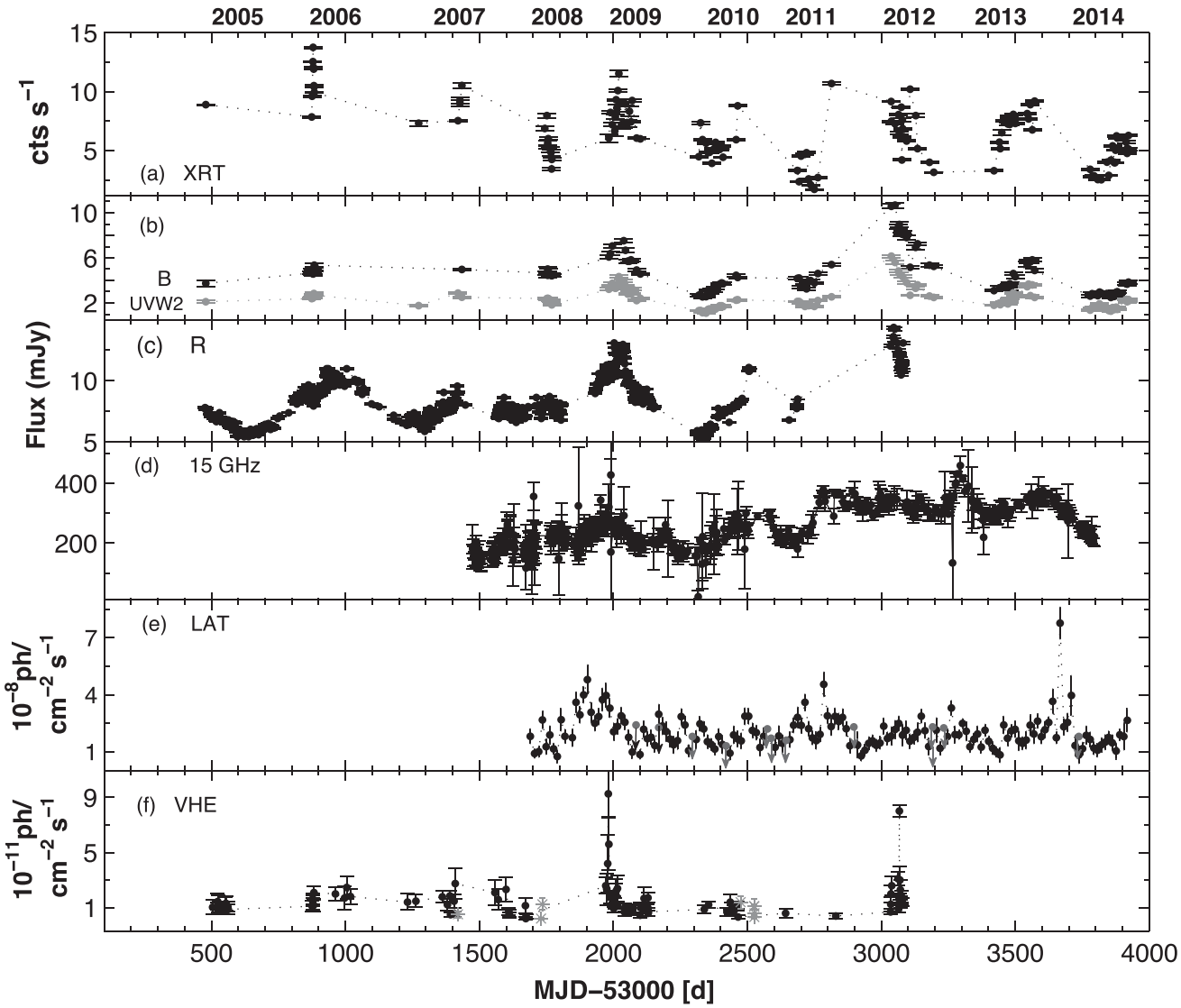

Figure 1. Historical 0.3–10 keV light curve from the XRT 2005–2013 observations (upper panel) and those constructed via the UV-optical (UVOT *B* and *UVW2* bands, Johnson–Cousin's *R* band; panels b and c, respectively), radio (OVRO; panel d), HE (LAT 0.3–100 GeV; panel e; grey colour is used for an upper limit to the flux) and VHE [MAGIC ($E > 300$ GeV, points), VERITAS ($E > 1$ TeV, asterisks); panel f] data obtained during the same period.

Table 3. Summary of the XRT and UVOT observations in different periods (Column 1). Column 2: number of X-ray flares in the given period; Columns 3–6: maximum 0.3–10 keV flux (in count s^{-1}), maximum-to-minimum flux ratio, and fractional rms variability amplitude (per cent) for each flare, respectively; Columns 7–8: maximum-to-minimum flux ratios for unabsorbed 0.3–2 keV and 2–10 keV fluxes; Columns 9–14: maximum-to-minimum flux ratios for the UVOT bands.

			XRT					UVOT					
Per.	Dates	N_{fl}	F_{max}	R	F_{var}	$R_{0.3-2}$	R_{2-10}	R_V	R_B	R_U	R_{UVW1}	R_{UVM2}	R_{UVW2}
(1)	(2)	(3)	(4)	(5)	(6)	(7)	(8)	(9)	(10)	(11)	(12)	(13)	(14)
1	2006 May 19–29	1	13.74	1.75	16.3(0.2)	1.62	2.12	1.14	1.17	1.17	1.14	1.19	1.19
2	2007 Jun 22–Nov 30	1	10.52	1.44	13.3(1.3)	1.83	1.73	–	–	1.07	1.36	1.63	1.63
3	2008 Oct 5–31	1	7.96	2.32	24.6(1.1)	2.61	3.19	1.20	1.14	1.56	1.33	1.33	1.32
4	2009 Jun 1–Sept 26	2	11.5, 9.23	1.60, 1.54	20.0(0.8), 13.9(0.9)	2.14	2.32	1.63	1.54	1.66	1.85	1.96	1.96
5	2010 May 2–Sept 24	2	7.34, 8.79	1.88, 1.49	21.4(0.5), 34.8(0.7)	2.12	3.27	1.82	1.75	2.66	2.66	2.00	2.06
6	2011 May 5–Sept 10	2	4.81, 10.89	2.83, 6.4	41.9(0.7), 97.9(1.1)	5.05	7.76	1.36	1.66	1.41	1.33	1.48	1.50
7	2012 Apr 19–Sept 26	1	10.20	3.24	28.8(0.4)	2.98	4.20	1.89	2.07	2.44	2.15	2.49	2.47
8	2013 May 8–Oct 7	1	9.18	2.80	20.4(0.4)	2.60	2.98	1.74	1.87	2.05	2.02	1.98	2.03
9	2014 May 2–Sept 22	1	6.26	2.49	24.2(0.4)	2.28	3.18	1.48	1.54	1.63	1.73	1.67	1.80

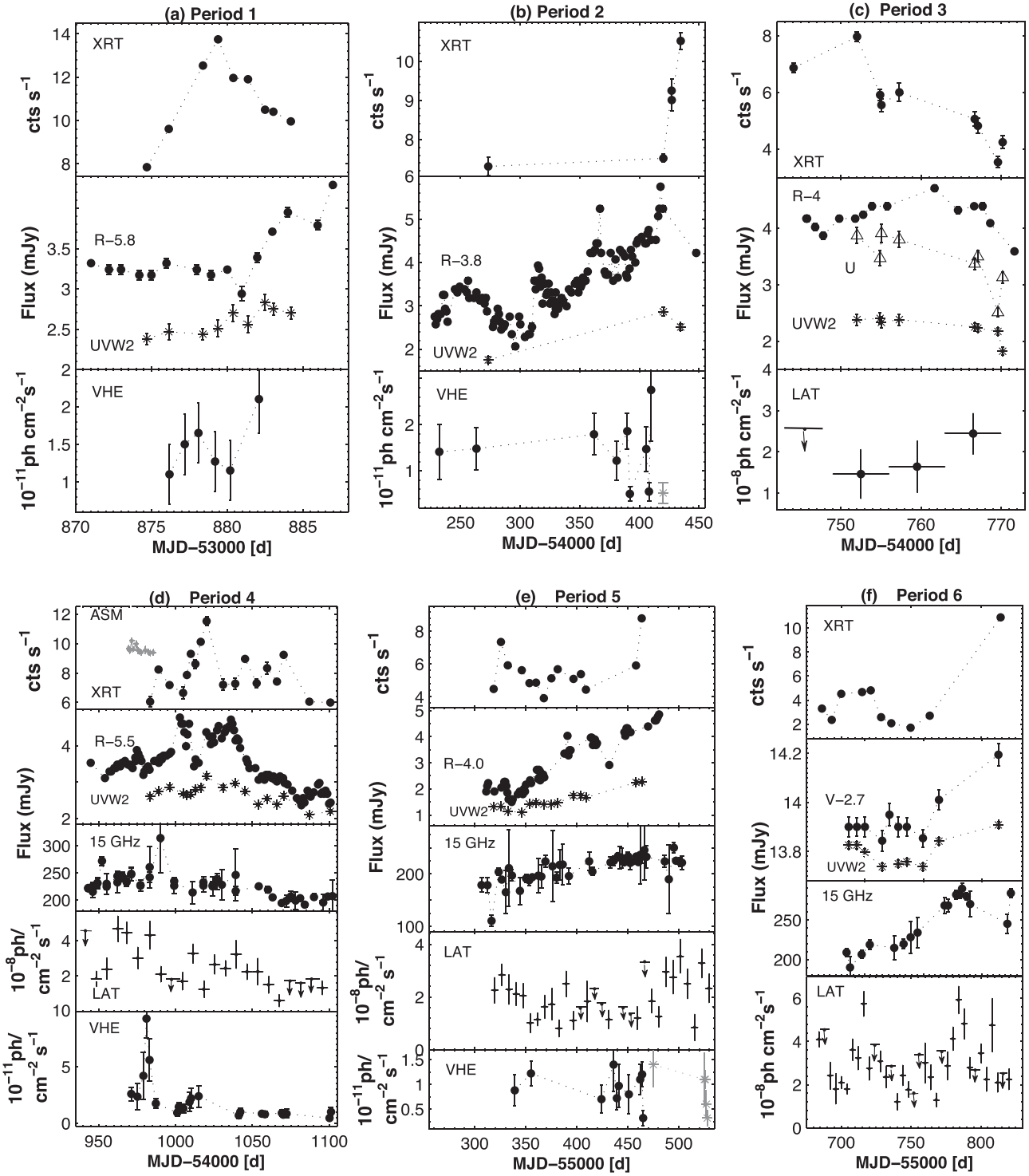

Figure 2. Multi-wavelength variability of 1ES 1959+650 in different epochs.

offset from the UV and X-ray ones (Fig. 2d). Furthermore, the source underwent a strong VHE outburst by a factor of ∼4 in 8 d and attained its highest level during the 2005–2012 period on May 30 (MJD 54981.32). The high 0.3–100 GeV brightness state was also observed in this epoch (4th panel). However, we do not observe a similar behaviour in the synchrotron part of the spectrum during these days. Although the 0.3–10 keV flux shows a short-term outburst by 10.5 per cent in this epoch, its peak is seen eight days later compared to that in the VHE band. The maximum 1.5–12 keV flux (from the *RXTE*-ASM observations, grey points in upper panel) was recorded on MJD 54571.54, followed by a decay in the following days, and, during the high VHE brightness state, the ASM-band flux was by 40–60 per cent lower compared to its maximum. A similar trend is seen from the densely sampled *R*-band light curve which exhibited its maximum a week earlier than the VHE peak. We also do not observe any significant activity at 15 GHz

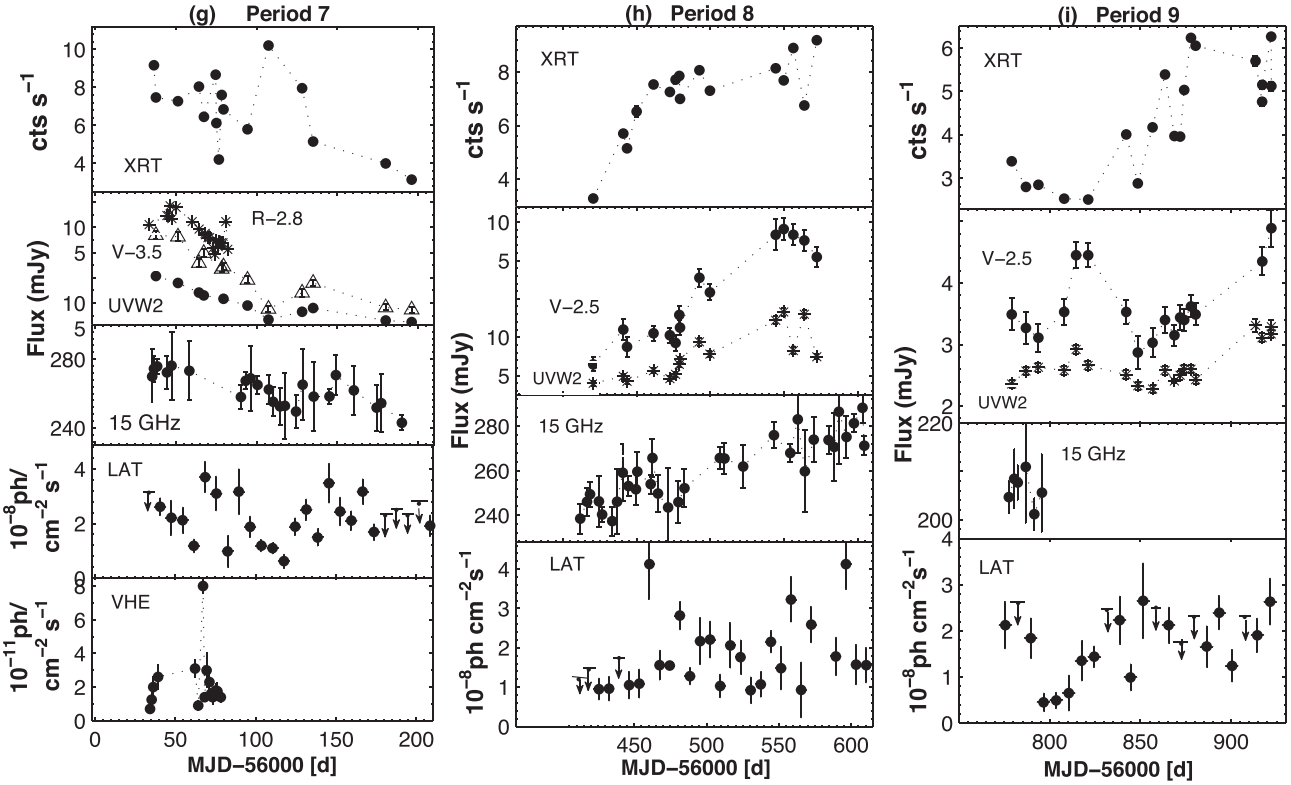

Figure 2 – *continued*

in this epoch (third panel). It is also remarkable that an increasing X-ray activity around MJD 55050 was not accompanied by those in the UVOT, *R* and LAT bands which show long-term decaying trends in this epoch. As for the VHE observations, the source showed its lowest level in this epoch. The correlated behaviour was observed only around MJD 55020 when 1ES 1959+650 underwent a sort-term outburst by a factor of 1.73 and reached its highest X-ray brightness state in this epoch.

3.3 The 2010–2013 observations

An X-ray flux increase by a factor of 1.64 in 7 d was observed at the beginning of Period 5 (see Table 3), followed by a much longer decay (Δt = 42 d; see Fig. 2e, upper panel). The *UVW2*-band light curve did not show a time shift whereas the *R*-band maximum was observed 4 d later (second panel). Similar to that from the *R* band, the 15 GHz light curve exhibited a long-term increase till MJD 55462.30 when the source showed another X-ray flare, reaching the highest 0.3–10 keV level for this period. The HE light curve showed its peaks in the epochs of highest optical–X-ray brightness states observed in the beginning and the end of this period (fourth panel). In Period 6 (see Table 3), we observe a short-term X-ray flare by a factor of ∼2 around MJD 55700 while the *UVW2*-band flux shows a decay and subsequent low level in this epoch (Fig. 2f, the upper and second panels). The 0.3–100 GeV light curve showed its first peak in the epoch of the first X-ray flare, while a low γ-ray flux level is observed when the source underwent the second 0.3–10 keV flare, and the source exhibited its second HE peak a month later after this event.

The source was in a high X-ray brightness level during the first half of Period 7 (see Table 3) when it showed two fast events when the 0.3–10 keV flux halved in 2 d and then increased by a factor of 2.5 in 1.7 d during MJD 56074.69−56078.43 (Fig. 2g, upper panel). We also observe increasing radio and VHE activities at the beginning of this period (the third and lower panels, respectively). The MAGIC observations revealed a fast VHE flare by a factor of ∼9 around MJD 56067 (2012 May), coinciding the first maximum of the LAT-band light curve in this period (4th panel). However, the contemporaneous XRT observation showed a dip and the source did not exhibit an increasing optical–UV activity during these days. Note that the radio–UV light curves showed the maximum on MJD 56039 (similar to the X-ray one), and then they followed a long-term decay trend till MJD 56107.36 when the source exhibited another short-term X-ray outburst. In this epoch, the LAT light curve (constructed with the weekly binned data) showed a behaviour similar to those of radio–UV light curves, and its maximum/minimum was recorded nearly the corresponding epochs of the latter. The source was in a flaring state during the majority of Period 8 (see Fig. 2h, upper panel) when the X-ray flux showed a slow increase by a factor of 2 in 40 d, and it then fluctuated around the 7.5 count s^{-1} level. The optical–UV and radio light curves followed that from the 0.3–10 keV band (the second and third panels, respectively). The highest 0.3–100 GeV flux level for this period was recorded in the epoch when the X-ray light curved showed a transition from a rise to a plateau-like behaviour. The next higher γ-ray brightness state coincided with the epoch of highest radio, optical–UV and X-ray states in this period.

Finally, 1ES 1959+650 showed a flare by a factor of 2.5 in Period 9 (see Table 3), and exhibited a higher brightness state during more than two months (superimposed by short-term flux fluctuations; Fig. 2h, upper panel)). A similar behaviour was observed also in the 0.3–100 GeV band where the one-week binning was used for a light curve construction (lower panel). The source showed two consecutive flares at the optical–UV frequencies (second panel).

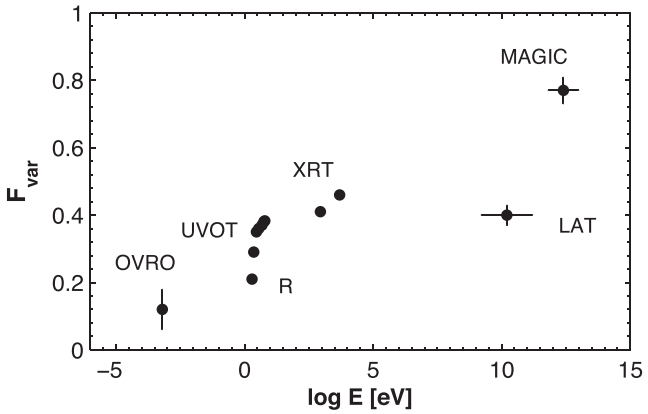

Figure 3. Fractional rms variability amplitude as a function of the energy for the 2005–2014 period.

However, the peaks of the corresponding light curves during the first event was recorded in the epoch when the source showed its lowest X-ray brightness state in this period, and the HE fluxes were also lower. In contrast, the second flare occurred in the epoch of high X-ray and HE brightness states.

3.4 $F_{\rm var}$ versus energy

If the fractional rms variability amplitude increases with the photon energy, this may be an indication of a significant spectral variability in the source (see Zhang et al. 2005, Vercellone et al. 2010). This trend was studied by different authors for PKS 2155−304 during the unprecedented VHE flare in 2006 July (Abramowski et al. 2010) as well for the multi-wavelength observations of this object in different epochs (Kapanadze et al. 2014, hereafter K14) using the following relation

$$F_{\rm var}(E) \propto E^{m}, \tag{3}$$

where E is the photon energy.[11] We first constructed the scatter plot in the $F_{\rm var}$–log E representation for our targets where $F_{\rm var}$ values in each band were calculated using the all available data obtained during the 2005–2014 period (see Fig. 3). For the VHE band, we used only the MAGIC observations ($E > 300$ GeV) which were the most numerous for our target. As for the VERITAS data provided in Aliu et al. (2013, 2014), they are few and the different energy threshold is used for a photon flux derivation (($E > 1$ TeV). For the XRT 0.3–2 keV and 2–10 keV bands, we used the values $E =$ 0.95 keV and $E = 4.98$ keV derived as the logarithmic mean energies in the corresponding energy bands adopting the prescription of Zhang et al. (2002). The horizontal positions and corresponding bars for the LAT and MAGIC data points are taken from Aleksic et al. (2015).

The plot generally shows an increasing trend of fractional amplitude with energy. An exception is the $F_{\rm var}$ value derived from the LAT observations. However, this is clearly related to the use of two-week bins used for the calculation of this quantity in the 0.3–100 GeV energy range. Using equation (1), we obtained $m =$ 0.043(0.017) for our target.[12] This relation has been also used for the multi-wavelength observations, performed in the periods, described in Sections 3.2 and 3.3. In this case, we used small time bins for the LAT data depending the TS values from the corresponding observations – from $\Delta T = 4$ d (Period 6) to $\Delta T = 7$ d (Periods 4, 5, 7–9).[13] We obtained the range $m = 0.04$–0.22 for different periods (see Table 4) that is mainly related to the use of different energy ranges for a construction of the corresponding scatter plots. For some periods, the OVRO, *R*-band, LAT or MAGIC data were not available. The VHE flux did not show a variability at 3σ confidence in Periods 1, 5, 6, and the same was for the 0.3–100 GeV flux in Period 3. The m parameter was small ($m < 0.3$) and comparable to its error in Period 2 and we have not included it in Table 4.

Table 4. The $F_{\rm var} \propto E^{\rm m}$ relation in different periods.

Period	Logarithm of freq. range (Hz)	m
1	14.67–18.08	0.22(0.01)
3	14.67–18.08	0.21(0.02)
4	10.18–26.40	0.07(0.02)
5	10.18–24.40	0.05(0.02)
7	14.67–26.60	0.04(0.02)
8	10.18–24.40	0.06(0.02)
9	14.74–24.40	0.05(0.02)

The trend of increasing fractional variability with energy was violated in Period 6 when the $F_{\rm var}$ value for the 15 GHz observations (12.7 ± 1.1 per cent) was higher than those from the *R, V, U* bands [8.0(0.3)–10.6(1.0) per cent] and slightly smaller than those from other optical–UV bands. At the higher energies, the variability in the 0.3–2 keV and 2–10 keV bands [$F_{\rm var} = 55.0(1.3)$–$81.6(1.6)$ per cent] significantly exceeded that observed in the LAT band ($37.2 \pm$ 4.3 per cent).

3.5 Intra-day variability

We have also performed an intensive search for an intra-day X-ray variability (IDV; i.e. a flux change within a day; see Wagner & Witzel 1995) using the χ^2-statistics introduced by Kesteven, Bridle & Brandie (1976). For 1ES 1959+650, we detected the 19 IDVs at the 99.9 per cent confidence (the threshold generally used for this purpose; see e.g. Andruchow, Romero & Cellone 2005). For each event, the values of reduced χ^2, and fractional variability amplitude, are provided in Table 5. The ranges of spectral parameters a, b and $E_{\rm p}$ (see Section 4 for their definitions) are also given along with each event, derived via the fit of the spectra extracted from the separate orbits of the corresponding observation with the log-parabolic spectral model.

The fastest event was recorded on 2013 June 18 (MJD 56461.37; see Fig. 4a) when the source showed two successive drops in the 0.3–10 keV count rate by 21–24 per cent, separated by an increase by 18 per cent. These fluctuations occurred in the course of about 1 ks. The source also showed a very fast variability with 1.32 ks during the third orbit of the 2006 May 23 pointing (MJD 53878.53) when the X-ray flux increased by 16 per cent (see Fig. 4c for the corresponding light curve). Note that this event was embedded in the longer IDV – the source shows two successive brightenings by

[11] We observe a strong linear correlation between the log $F_{\rm var}(E)$ and log E quantities with the slope m.

[12] A caveat related to Fig. 3: given that blazars have broad-band Fourier spectra, this figure is also dependent on the very different sampling times and observation durations from the different experiments.

[13] For the calculation of fractional variability amplitude, we used only the flux values from those time bins when the source was detected above the 3σ significance.

Table 5. Extract from the summary of IDVs at the 99.9 and 99.5 per cent confidences from the *Swift*–XRT observations of 1ES 1959+650. Columns 4, 5, 6 give the ranges of the photon index at 1 keV, curvature parameter and the location of synchrotron SED peak derived by means of the fit of the spectra extracted from the separate orbits of the corresponding observation with the log-parabolic spectral model.

Obs. start–end (UTC) (1)	χ^2(d.o.f.) (2)	$F_{\rm var}$(per cent) (3)	a (4)	b (5)	$E_{\rm p}$ (keV) (6)
		99.9 per cent confidence			
2005-04-19 01:05:45 04–19 14:01:45	5.108/8[a]	3.23(0.56)	2.01(0.03)–2.16(0.04)	0.20(0.09)–0.40(0.08)	0.53(0.09)–0.97(0.08)
2006-05-23 10:09:53 05–23 15:16:53	2.515(89)	5.31(0.53)	1.87(0.02)–1.99(0.02)	0.20(0.04)–0.33(0.05)	1.09(0.08)–1.63(0.07)
2006-05-23 14:99:53 05–24 10:41:23	12.307(1[a])	4.29(0.99)	1.97(0.02)	0.28(0.04)	1.13(0.05)
2006-05-24 16:58:23 05–25 10:45:01	3.809(15[b])	3.70(0.80)	1.83(0.03)–1.99(0.02)	0.20(0.04)–0.32(0.06)	1.09(0.05)–1.84(0.08)
2006-05-25 10:35:01 05–25 23:36:23	2.588(76)	6.55(1.04)	1.79(0.04)–1.97(0.03)	0.28(0.06)–0.31(0.07)	1.13(0.07)–1.73(0.08)

Notes.[a]Orbit-binned fluxes.
[b]The 180 s binning.

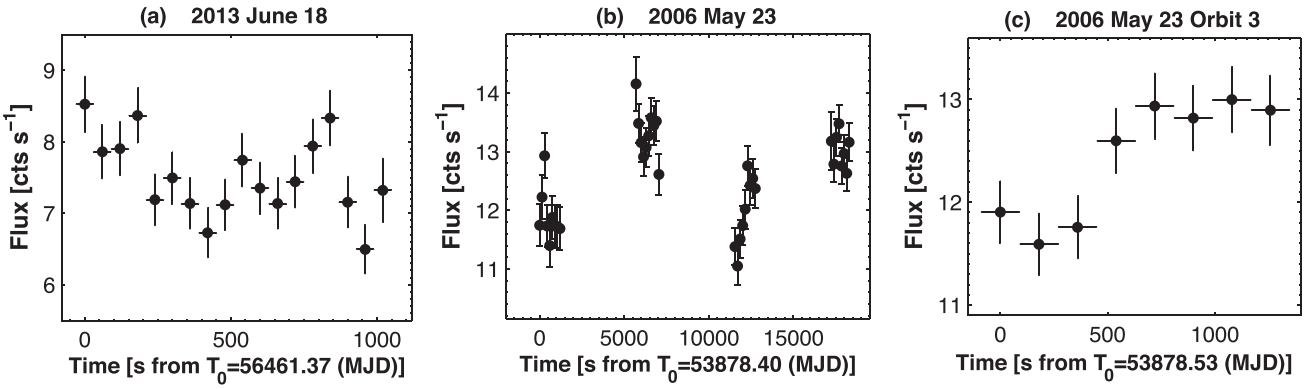

Figure 4. Light curves from the observations with IDVs at the 99.9 per cent confidence (extract).

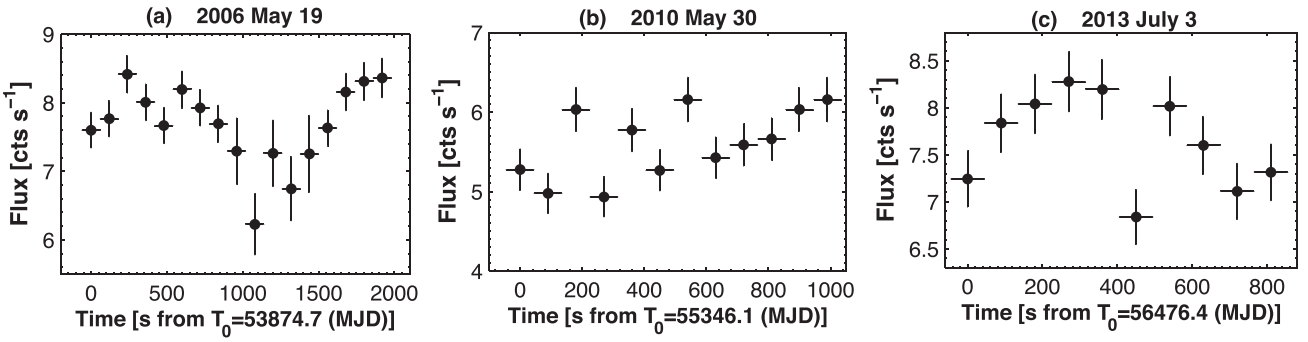

Figure 5. Light curves from the observations with IDVs at the 99.5 per cent confidence (extract).

17–1.24 per cent during 18.3 ks, separated by a drop by 19 per cent in $\Delta t \sim 4.8$ ks (Fig 4b).

The source was highly variable by $F_{\rm var} \approx 9.2$ per cent within about 17 ks on 2009 August 23 (MJD 55066.01; Fig. 4d), and it also showed a variability at the 99.5 per cent confidence level (so-called possible variability; see Andruchow et al. 2005) within the first orbit of this pointing (Fig. 4e) when the 0.3–10 keV count rate decayed by 22 per cent in 840 s.

One of the highest values of the $F_{\rm var}$ parameter was recorded during the 2012 May 27/28 (MJD 56074.69) observation when the X-ray flux dropped by a factor of about 40 per cent during 42 ks (Fig. 5f). Among the pointings consisting of five to nine orbits, the source showed an interesting behaviour on 2005 April 19 (MJD 53479.05) when the orbit-binned flux underwent two consecutive decay and increase by 4–8 per cent in the course of 46.5 ks (Fig. 5g). A similar behaviour was the case during the 2006 May 27 pointing (MJD 53882.52), split into eight orbits (Fig. 5h).

Among other events, the 2014 July 10 observation is notable with its fractional amplitude that is the largest for the X-ray IDVs in 1ES 1959+650, and the source showed a flux variability at 95 per cent during the second orbit lasting 360 s (Fig. 4j). A similar case was with the second orbit of the 2009 July 4 observation when the source showed an IDV with $F_{\rm var} = 12.1$ per cent within 7 ks (Fig. 7k).

Note that the source also showed an IDV from the VERITAS 2012 May 20 observations (MJD 56067.38; Fig. 4l, constructed via the data provided in Aliu et al. 2014) by $F_{\rm var} = 36$ per cent within 7ks. The VHE photon flux increased by a factor of 2.35 in about 1.8 ks and then showed a decay by a factor of 5.8 in the same time. Between these events, the source exhibited a marginal variability

Table 6. Extract from the summary of the XRT spectral analysis with log-parabolic model. The E_p values (Column 4) are given in keV; unabsorbed 0.3–2 keV, 2–10 keV and 0.3–10 keV fluxes (Columns 7–9) in erg cm^{-2} s^{-1}.

Obs Id (1)	a (2)	b (3)	E_p (4)	K (5)	χ^2/d.o.f. (6)	log $F_{0.3-2\,keV}$ (7)	log $F_{2-10\,keV}$ (8)	log $F_{0.3-10\,keV}$ (9)	HR (10)
35025001 Orbit 1	2.16(0.04)	0.29(0.08)	0.53(0.09)	0.076(0.001)	0.975/149	−9.640(0.011)	−9.936(0.022)	−9.462(0.011)	0.506(0.029)
35025001 Orbit 2	2.05(0.03)	0.28(0.08)	0.81(0.09)	0.070(0.001)	0.855/109	−9.682(0.010)	−9.896(0.022)	−9.475(0.011)	0.611(0.034)
35025001 Orbit 3	2.01(0.03)	0.34(0.07)	0.97(0.08)	0.073(0.001)	1.036/170	−9.674(0.010)	−9.879(0.019)	−9.463(0.010)	0.624(0.031)
35025001 Orbit 4	2.12(0.03)	0.40(0.08)	0.71(0.09)	0.076(0.001)	0.877/167	−9.647(0.010)	−9.947(0.021)	−9.470(0.010)	0.501(0.027)
35025001 Orbit 5	2.13(0.04)	0.25(0.08)	0.55(0.10)	0.071(0.002)	1.050/133	−9.670(0.013)	−9.936(0.023)	−9.482(0.012)	0.542(0.033)

(with the confidence below 2σ during 2.4 ks). If we define the flux doubling time as (Saito et al. 2013)

$$\tau_d = \frac{\Delta t \times \ln 2}{\ln(F_2/F_1)}, \quad (4)$$

we obtain $T_2 = 1.47 \pm 0.25$ ks, or equivalently the exponential growth time-scale

$$\tau_{exp} = \frac{\tau_d}{\ln 2}, \quad (5)$$

that equals 2.12 ± 0.35 ks for this event. Although there was a contemporaneous XRT observation (plotted with the asterisks in the same panel), its duration was too short (675 s) and the 0.3–10 ks shows a variability of only about 90 per cent confidence ($\chi^2_r = 1.558$ with 10 d.o.f.). Probably, the X-ray variability time-scale was larger compared to this interval and a significantly longer exposure was necessary to detect an IDV.

We have found the seven cases of a possible variability whose summary is also given in Table 5. The source showed a successive flux decay and increase by $F_{var} \approx 6.2$ per cent within about 1.7 ks on 2006 May 19 (MJD 53874.67; see Fig. 5a). A flux increase by 23 per cent in about 1 ks was recorded on 2010 May 30 (MJD 55346.12; Fig. 5b). The source also showed fluctuations by the fractional amplitude of 5.1 per cent within 0.9 ks in the case of the 2013 July 3 (MJD 56474.37) pointing (Fig. 5c).

Our timing study of long-term XRT monitoring of 1ES 1959+650 shows that the source was highly variable on longer (weeks-to-months) time-scales with the 0.3–10 keV fluxes ranging by a factor by a factor of 2–7, and it showed X-ray IDVs characterized by fractional variability amplitudes of 3.1–19.3 per cent (see the corresponding discussion in Section 6.1). The timing behaviour exhibited an erratic character in this object and no signatures of periodic variations are revealed.

4 SPECTRAL ANALYSIS

We performed the spectral analysis by fixing the N_H absorbing column density to the Galactic value and using the log-parabolic model (LP; Massaro et al. 2004, hereafter M04)

$$F(E) = K(E/E_1)^{(-a+b\log(E/E_1)} \text{ ph cm}^{-2}\text{ s}^{-1}\text{ keV}^{-1}, \quad (6)$$

with E_1 the reference energy, generally fixed to 1 keV, a the photon index at the energy E_1, b the curvature parameter, and K the normalization factor. The values of these parameters are derived during the fit process. The location of SED peak is given by

$$E_p = E_1 10^{(2-a)/2b}. \quad (7)$$

This parameter can be directly derived with the alternative form of log-parabola model, along with E_p and b (LPEP; Tramacere et al. 2009; hereafter T09)

$$S(E) = 1.6 \times 10^{-9} S_p 10^{-b(\log(E/E_p)^2)} \text{ erg cm}^{-2}\text{ s}^{-1}, \quad (8)$$

Table 7. Distribution of different spectral parameters: minimum and maximum values (Columns 2 and 3, respectively), distribution peak (Column 4) and variance (last column).

Quantity (1)	Min. (2)	Max. (3)	Peak (4)	σ^2 (5)
a	1.76	2.37	2.02	0.016
HR	0.317	0.918	0.550	0.013
b	0.18	0.67	0.35	0.010

where S_p is the SED peak height. This quantity can be also calculated via the LP model as (M04)

$$\nu_p F(\nu_p) = 1.6 \times 10^{-9} K 10^{(2-a)^2/4b)} \text{ erg cm}^{-2}\text{ s}^{-1}, \quad (9)$$

which is related with the synchrotron bolometric flux as

$$F_{bol} = 2.70 \frac{\nu_p F(\nu_p)}{\sqrt{b}}. \quad (10)$$

We fixed the equivalent hydrogen column density to the weighted mean value $N_H = 1.00 \times 10^{21}$ cm^{-2}, derived via the Total Galactic H I Column Density Calculator[14] using the Leiden/Argentine/Bonn (LAB) Survey of Galactic H I (Kalberla et al. 2005). For each spectrum, the model validity was checked by means of reduced chi-square, distribution of the residuals, and F-test. Generally, the single power law (see below) was excluded at the 99.99 per cent significance or the LP model was clearly preferred by the aforementioned tests (for 184 out of 187 spectra, including those from the separate orbits of a single observation when it was impossible to use the same source and background extraction regions for all orbits, or the source showed a flux variability during this observation). The latter also gave better statistics compared to LPEP.[15] The results of the spectral analysis performed with the LP model are provided in Table 6. The hardness ratio (HR) is calculated as the ratios of unabsorbed 2–10 keV to 0.3–2 keV fluxes. In Table 7, we present the properties of the distribution of the a, HR, b parameters. The distribution peaks are derived via the lognormal fit to the corresponding histograms (see Fig. 6). Generally, this source showed the curved spectra – about 81 per cent out of the values of the b parameter are included in the interval 0.25–0.50 from their broad range $\Delta b = 0.49$ (Fig. 7a). Table 6 also includes the values of the spectral curvature detected at the 2σ and even above 1σ confidences (less than 15 per cent of the curved spectra) when the power law was rejected by the tests (although the latter are not used for a construction of the distribution of this parameter). Note that these values

[14] http://heasarc.gsfc.nasa.gov/cgi-bin/Tools/w3nh/w3nh.pl

[15] The latter also showed a systematic shift of the E_p parameter to higher values when $E_p \lesssim 1.2$ keV (compared to those calculated via equation 4) – sometimes to beyond 2 keV, and towards lower energies – for the spectra with $E_p \gtrsim 1.5$ keV. Therefore, we have not used these results in our analysis.

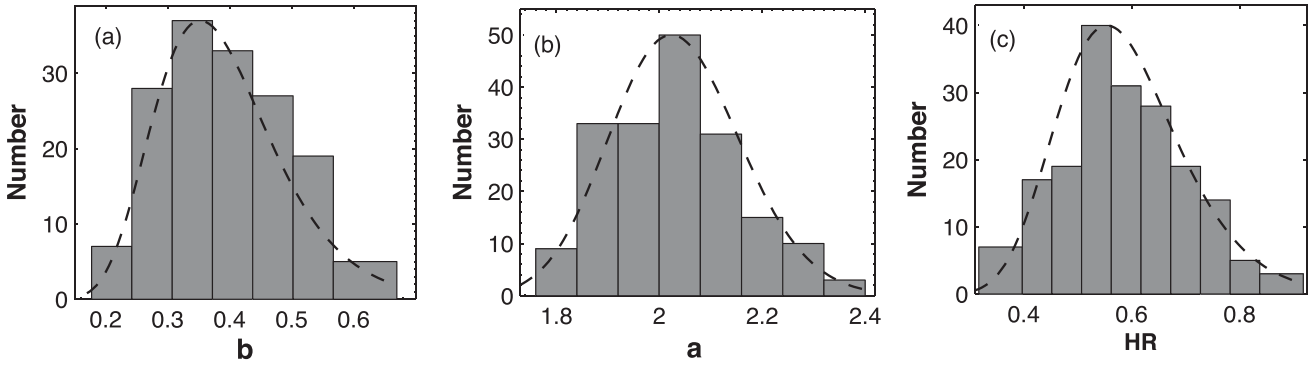

Figure 6. Distribution of the values of different spectral parameters: curvature parameter, HR and photon index at 1 keV. The dashed lines represent the lognormal fit to the distributions.

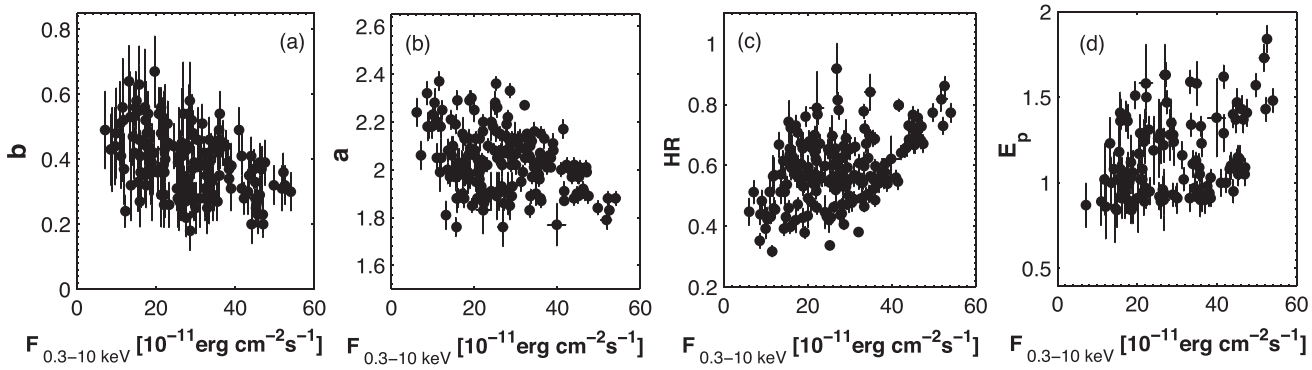

Figure 7. Correlation between different spectral parameters and fluxes (extract).

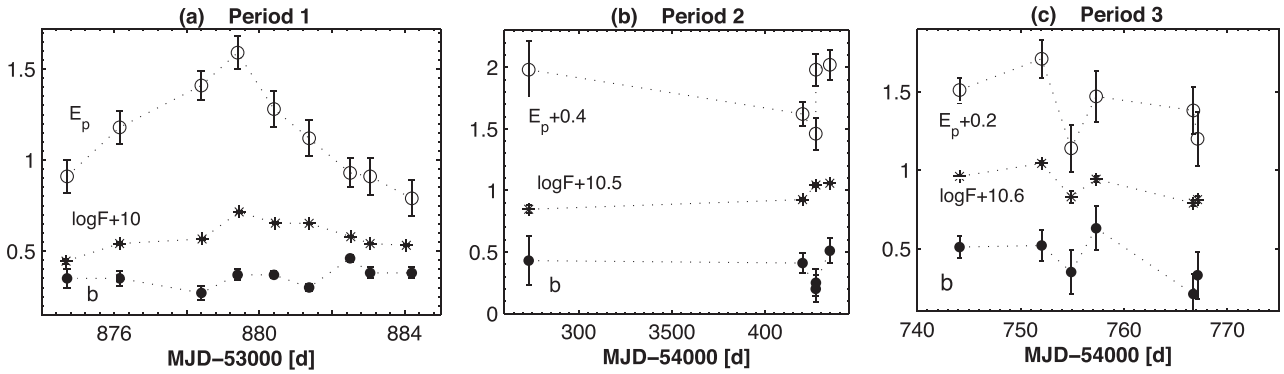

Figure 8. 0.3–10 keV fluxes, curvature parameter and E_p plotted versus time for different long-term flares and IDVs (extract). The points with an arrow stand for the upper limits to the E_p parameter.

are mostly derived from relatively poor spectra – their degrees of freedom are less than 85 that yields to higher uncertainties compared to richer spectra (i.e. those with d.o.f.), and the detection of the spectral curvature below the 2σ significance.

This parameter showed an anti-correlation with the 0.3–10 keV model flux (see Fig. 8a and Table 9 for the Pearson correlation coefficient and corresponding p-value). The mean value of the curvature parameter $\bar{b}$ ranged between 0.34 and 0.42 for the observations corresponding to a higher X-ray brightness state in Periods 1, 5, 7–9. The spectral curvature showed an evolution mainly opposite to that of the 0.3–10 keV flux in Periods 1–2, 2009 June–July (MJD 54983.58−55038.93), 2010 May–August (55318.54−55409.02), 2011 May–July (55686.17−55763.44), 2012 April–July (56036.56−56135.10), Periods 8–9. However, a large scatter of data points in Fig. 8(a) shows that the anti-correlation was not always the case for our target. Namely, no dominant trend or the b parameter shows a positive correlation with a flux variability during the IDVs of 2006 May 23–28, 2012 May 27/28 and longer-term events observed in Period 3, 2009 July–September (MJD = 55013.02−55100.69). Note that $b > 0.50$ for the 13 spectra with the unabsorbed 0.3–10 keV model fluxes higher than 2.1×10^{-10} erg cm^{-2} s^{-1} (the weighted mean 0.3–10 keV flux in the 2005–2014 period).

As for the a parameter, it also showed a wide range of the values $\Delta a = 0.61$ whose 39.1 per cent are lower than $a = 2.00$ (Fig. 6b). The hardest spectra are found in Period 1–3, 5 with the mean value $\bar{a}$ ranging between 1.91 and 1.98. The source is significantly softer in Period 4, 6–8 with $2.09 \leqslant \bar{a} \leqslant 2.14$. The spectra with $a \leq 1.90$

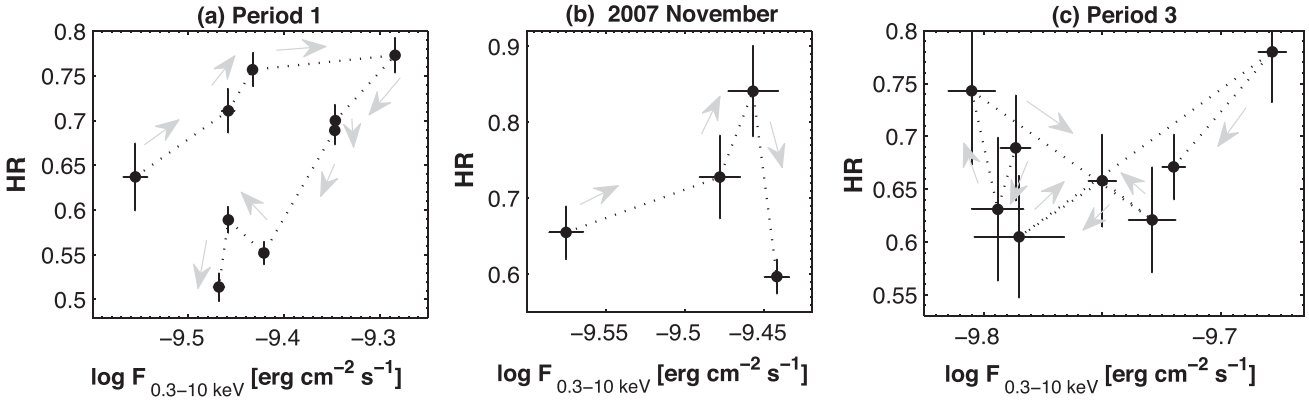

Figure 9. HR – 0.3–10 keV flux planes corresponding to different long-term X-ray flares and IDVs (extract).

mostly correspond to the 0.3–10 keV flux values higher than 2.50 $\times$ 10^{-10} erg cm^{-2} s^{-1} while for the softest spectrum $F_{0.3-10\,\mathrm{keV}} = (1.16 \pm 0.05) \times 10^{-10}$ erg cm^{-2} s^{-1}, and $a \geq 2.20$ for the pointings with the $F_{0.3-10\,\mathrm{keV}}$ quantity mainly below the aforementioned mean weighted value. Fig. 7(b) shows a moderate, statistically significant anti-correlation between a and 0.3–10 keV model flux, revealing that the source followed mainly a 'harder-when-brighter' trend.

The HR parameter also showed a wide range of $\Delta\mathrm{HR} = 0.488$ (Fig. 6c, including the values derived from the spectra fitted with the power-law model), and its positive correlation with the 0.3–10 keV flux confirms the dominance of a 'harder-when-brighter' evolution of the flares (Fig. 7c). In the HR-flux plane, a pure clockwise (CW) evolution occurred in 2010 May–June period (MJD = 55318.54–55367.66; Fig. 9c). A mostly CW evolution occurred during the flares of Period 1, 2009 June–July (54983.58–55038.93), 2010 June–August (55375.14–55458.13), 2011 May–July (55686.17–55763.44), 2012 April–July (56036.51–56135.10), Period 8, Period 9, and the changes to an opposite trend are mainly related to the short-term outbursts superimposed on the longer variable event (see Fig. 9). Note that the hardest spectrum with $a = 1.76 \pm 0.08$, HR $= 0.918 \pm 0.084$ belongs to the 2008 October 13 (MJD 54752.03) observation when the source was in a relatively high X-ray state ($F_{0.3-10\,\mathrm{keV}} = 2.69 \times 10^{-10}$ erg cm^{-2} s^{-1}) while lowest value of the HR quantity is obtained from the 2011 May 15 pointing (MJD = 55686.17) that belongs to the epoch of a target's faint state ($F_{0.3-10\,\mathrm{keV}} = 1.16 \times 10^{-10}$ erg cm^{-2} s^{-1}). The source did not show a pure opposite trend during any flare. In the case of IDVs, the a parameter showed a variability at 3σ (2006 May 23) and 2σ (2005 April 19, 2006 May 27) confidence levels. The spectral evolution followed mainly a CW trend during the 2005 April 19 event, and no dominant trend was seen in other cases.

The position of the SED peak was always found in the soft X-ray part of the spectrum, and they range between 0.12 and 1.84 keV. However, when $E_\mathrm{p} \lesssim 0.80$ keV, the E_p value derived from the X-ray spectral analysis is systematically higher than that obtained from the broad-band SEDs via the following log-parabolic function (introduced by Landau et al. 1986)

$$\log \nu F_\nu = A(\log \nu)^2 + B(\log \nu) + C, \quad (11)$$

or with the cubic relation introduced by Comastri, Molendi & Ghisellini (1995)

$$\log \nu F_\nu = a(\log \nu)^3 + b(\log \nu)^2 + c(\log \nu) + d, \quad (12)$$

i.e. the intrinsic position of the synchrotron SED peak is poorly constrained by the XRT observation. Therefore, these E_p values should be considered as upper limits to the intrinsic ones (see K14), and we did not use them when searching for the correlations between the E_p and other spectral parameters or fluxes. This was the case for 38 per cent of the spectra, and, therefore, we have not constructed the distribution of the E_p parameter. On the other hand, the errors associated with the log ν_p values (defined as $\nu_\mathrm{p} = E_\mathrm{p}/h$) derived from the broad-band SEDs can be as high as 0.5 when we do not have strictly simultaneous radio observations or the UVOT performed its observation only in one band out of six along with that of XRT (see K14). Consequently, we cannot construct the distribution of this parameter and the study of a time variability of the E_p along with the 0.3–10 keV flux has been performed only for those longer-term flares or IDVs that showed mostly the spectra with $E_\mathrm{p} \geq 0.80$ keV.

The E_p parameter showed a very weak positive correlation between E_p and the 0.3–10 keV flux (Fig. 8d). The evolution of E_p (see Fig. 9) mainly followed that of the total flux during Period 1 (with the range $\Delta E_\mathrm{p} = 0.81$ keV),[16] Period 3 (0.57 keV), 2010 May–June (55318.54–55367.66; 0.39 keV), and no clear trend is seen for other periods. The highest value of this parameter is found for the spectrum extracted from the first orbit of the 2006 May 24 (MJD 53879.44) pointing corresponding to one with the highest historical 0.3–10 keV unabsorbed flux. However, the upper limits to the synchrotron SEDs did not show clear trends, and 66 per cent of them belong to the epochs when the unabsorbed flux was higher than its mean historical value. In the case of IDVs with the number of the orbits higher than 4, E_p does not show a positive correlation with the flux, and we observe mainly an opposite evolution during the 2006 May 23 (MJD 53878.42) pointing. It varied by $\Delta E_\mathrm{p} = 0.34$–$0.77$ keV during different IDVs (see the last column of Table 5). The largest variability occurred during the 2012 May 27–28 event when the 0.3–10 keV count rate also showed one the largest fractional variability amplitude. Similar to M08, we examined a relation between E_p and $S_\mathrm{p}(L_\mathrm{p})$ quantities, and revealed a very weak positive correlation between them.[17] No positive results were

[16] For each Obs ID, the corresponding E_p is a weighted mean value from those derived from the spectra extracted from separate orbits.

[17] Although the relatively well sampled IDVs and longer-term flares exhibit, in average, a positive trend in the $S_\mathrm{p}(L_\mathrm{p})$ values with the increasing E_p quantity, the scatter of corresponding data points is large and does not show a statistically significant cross-correlation.

Table 8. Summary of the XRT spectral analysis with a simple power-law model. The quantities are given in the same units as in Table 6.

Obs Id	Γ	K	χ^2/d.o.f.	$F_{0.3-2\,\mathrm{keV}}$	$\log F_{2-10\,\mathrm{keV}}$	$\log F_{0.3-10\,\mathrm{keV}}$	HR
(1)	(2)	(3)	(4)	(5)	(6)	(7)	(8)
00035025014	2.09(0.05)	0.065(0.002)	1.009/53	−9.696(0.017)	−9.83490.028)	−9.478(0.013)	0.728(0.055)
00035025020	2.15(0.04)	0.038(0.002)	1.105/45	−9.919(0.015)	−10.101(0.025)	−9.699(0.012)	0.658(0.044)
00035025025	2.12(0.05)	0.031(0.001)	1.131/39	−10.000(0.016)	−10.162(0.027)	−9.773(0.013)	0.689(0.050)

obtained when searching for a correlation between E_p and b (see the corresponding discussion in Section 6.2).

Using equation (7), we calculated the bolometric synchrotron fluxes from the XRT observations which range between 7.8×10^{-11} erg cm^{-2} s^{-1} and 7.37×10^{-10} erg cm^{-2} s^{-1}. Adopting a flat cosmology with $H_0 = 69.6$ km s^{-1} Mpc^{-1} and $\Omega_M = 0.3$, the corresponding isotropic luminosities fall within the interval (0.58–5.46) $\times 10^{45}$ erg s^{-1}.

Only three spectra out of 187 were fitted better with a single power-law model, given by

$$F(E) = KE^{-\Gamma}, \tag{13}$$

where the units of the normalization factor K are photons cm^{-2} s^{-1} keV^{-1}, E is the photon energy (in keV), and Γ is the photon index throughout the observation band (see Table 8 for the results). These spectra show $\Gamma = 2.09$–2.15 and HR = 0.689–0.728. Note that the corresponding optical–UV are significantly lower compared to those from the XRT band [$F_{\mathrm{opt\text{-}UV}} = (2.42$–$3.50) \times 10^{-11}$ erg cm^{-2} s^{-1} versus $F_{0.3-2\,\mathrm{keV}} = (1.00$-$1.21) \times 10^{-10}$ erg cm^{-2} s^{-1}], and the better statistics for the power-law fit compared to the LP one cannot be related to presence of the synchrotron SED peak far from the instrumental range of the XRT that, on its turn, makes it difficult to evaluate a possible curvature, and the simple power-law model gives relatively better description of the spectrum (see Massaro et al. 2008; K14).

Finally, we have not found any indication of the contribution of the photons of IC origin to the 0.3–10 keV spectra that may result in the appearance of an upward curvature ($b < 0$) and in a trend of increasing positive residuals above $\backsim$4–5 keV (see Zhang 2008).

Our spectral study shows that the X-ray spectra of 1ES 1959+650 are mainly curved with broad ranges of photon index, curvature parameter, HR and synchrotron SED peak location which exhibit significant variability with the flux at different time-scales. The source mainly showed a harder-when-brighter evolution in a HR-flux plane during different X-ray flares, although the changes to an opposite trend were also observed.

5 INTER-BAND CROSS-CORRELATIONS

The soft (0.3–2 keV) and hard (2–10 keV) X-ray fluxes from the 2005–2013 observations of 1ES 1959+650 are plotted versus time in Fig. 10(a). The former varied between $(4.22 \pm 0.27) \times 10^{-11}$ erg cm^{-2} s^{-1} and $(3.05 \pm 011) \times 10^{-10}$ erg cm^{-2} s^{-1}. In the case of hard X-ray flux, we obtained the range of (0.19–2.43) $\times 10^{-10}$ erg cm^{-2} s^{-1}. Note that the lower 2–10 keV fluxes of (0.84–1.40) $\times 10^{-11}$ erg cm^{-2} s^{-1} were obtained from the *RXTE*–PCA 2000 July–September observations of our target (Giebels et al. 2002). The low hard X-ray fluxes of (1.04–1.29) $\times 10^{-11}$ erg cm^{-2} s^{-1} were also reported by Beckmann et al. (2002) from the *BeppoSAX* pointing of 1997 May 4–5, and by Tagliaferri et al. (2003) from the *ROSAT* 1996 March 31 observation. The highest historical level of the 2–10 keV flux of 2.9×10^{-10} erg cm^{-2} s^{-1} was reported by Perlman et al. (2005) from the *XMM–Newton* pointing of 2002 November 23. However, this result should be treated with caution since it was obtained using the single power law, and the corresponding reduced Chi-square does not show a good fit between the model and observed spectrum ($\chi^2_r = 1.44$ with 58 d.o.f.).

We see that these fluxes basically show a highly correlated behaviour. This is also evident from Fig. 10(b) where the 2–10 keV fluxes are plotted versus those from the 0.3–2 keV band. There is a strong correlation between these quantities (see Table 9). However, they were not always correlated. For example, the hard flux increased by a factor of 1.49 between MJD 55700.01 and MJD 55714.95 while the source showed a decay by a factor of 1.03 in the 0.3–2 keV energy band. This fact was related to the spectral hardening by $\Delta a = 0.31 \pm 0.06$ between these observations. Generally,

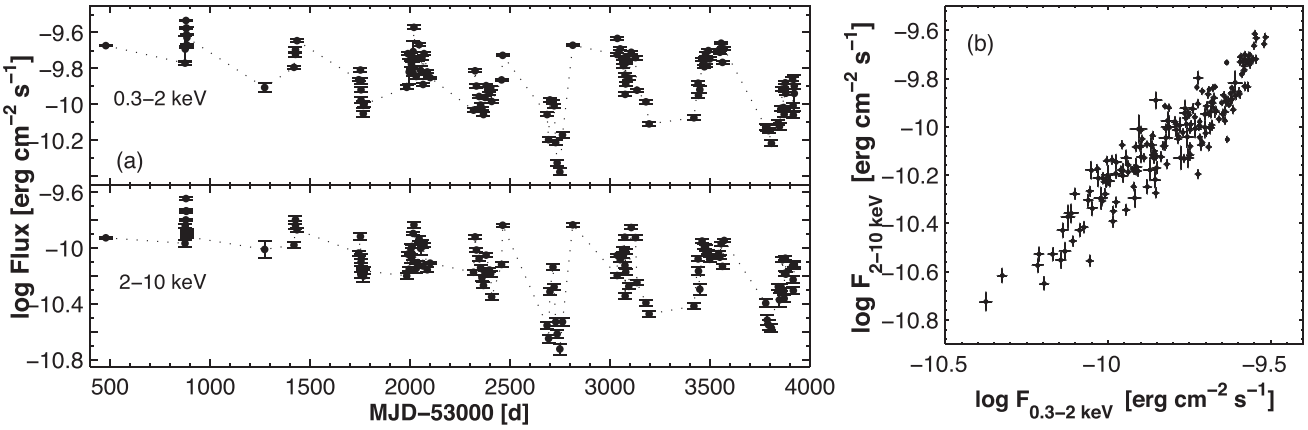

Figure 10. Cross-correlation between the soft (0.3–2 keV) and hard (2–10 keV) fluxes. The first figure shows a variability of these fluxes with time during 2005–2013, and the correlation between them is shown in the second panel of upper row. In the second row, the evolution of hard and soft fluxes with time and corresponding DCF plots are shown for the different XRT pointings (exhibiting IDVs). The solid lines represent a polynomial fit to the DCFs.

Table 9. Correlations between different spectral parameters and multi-band fluxes (extract).

Quantities	r	p
b and $F_{0.3-10\,\mathrm{keV}}$	−0.31(0.10)	9.51×10^{-5}
a and $F_{0.3-10\,\mathrm{keV}}$	−0.32(0.10)	5.15×10^{-5}
a and $F_{2-10\,\mathrm{keV}}$	−0.51(0.08)	5.90×10^{-7}
HR and $F_{0.3-10\,\mathrm{keV}}$	0.41(0.09)	1.50×10^{-8}
E_p and $F_{0.3-10\,\mathrm{keV}}$	0.21(0.12)	2.10×10^{-3}
E_p and S_p	0.23(0.12)	1.68×10^{-3}
$F_{0.3-2\,\mathrm{keV}}$ and $F_{2-10\,\mathrm{keV}}$	0.71(0.05)	4.10×10^{-12}

the hard X-ray flux showed a higher variability compared to the soft one – the maximum-to-minimum flux ratio R is equal to 12.88 for the 2–10 keV energy band while $R = 7.23$ for the soft X-ray band during the 2005–2014 period. The higher variability in the hard X-rays was always the case for all periods discussed in Sections 3.1–3.2, except for Period 2 (that can be caused by a poor data sampling compared to the other periods), and the ratio $R_{2-10\,\mathrm{keV}}/R_{0.3-2\,\mathrm{keV}}$ was the highest (1.54) in Periods 5–6 (see Columns 6–7 of Table 3).

In Fig. 11, we provide the examples of a time variability of the soft 0.3–2 keV and hard 2–10 keV unabsorbed X-ray fluxes from the XRT observations of 1ES 1959+650 where each point corresponds to the spectrum extracted from a separate orbit. The hard and soft X-ray light curves follow each other closely, and we have found a possible soft lag $\tau_\mathrm{soft} \approx 6.0 \pm 1.5$ ks from the 2005 April 19 observation using the discrete correlation functions (DCF) defined for each time lag τ as (Edelson & Krolik 1988)

$$\mathrm{DCF}(\tau) = \frac{1}{M} \sum UCDF_{i,\mathrm{j}}(\tau), \tag{14}$$

where the set of unbinned discrete correlations between the a and b time series is given by

$$UCDF_{i,\mathrm{j}} = \frac{(a_i - \bar{a})(b_\mathrm{j} - \bar{b})}{\sqrt{\sigma_a^2 \sigma_\mathrm{b}^2}}. \tag{15}$$

Here, a_i and b_j are the points of the a and b sets, respectively; $\bar{a}$ and $\bar{b}$ – their mean values; σ_a^2 and σ_b^2 – the variance of each set; M – number of pairs for the given time lag. However, the recent simulations of Max-Moerbeck et al. (2014) revealed different drawbacks of the DCF method, and they recommended to search for the cross-correlations between the two time series via the local

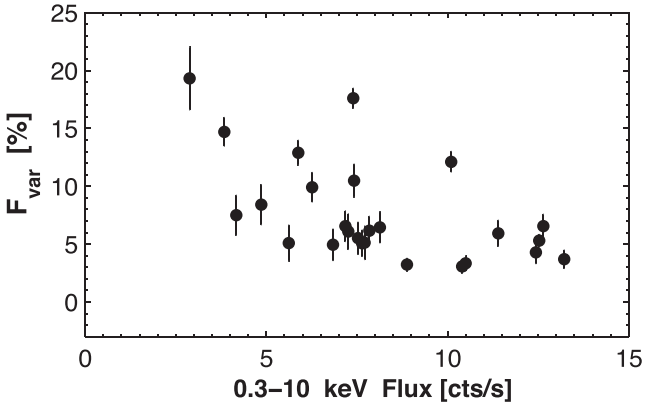

Figure 12. Fractional rms variability amplitude as a function of the XRT flux for the 2005–2014 period.

cross-correlation function (LCCF) defined as

$$\mathrm{LCCF}(\tau) = \frac{\sum (a_i - \bar{a_\tau})(b_\mathrm{j} - \bar{b_\tau})}{\sigma_{a\tau}\sigma_{\mathrm{b}\tau}}, \tag{16}$$

where the local mean values of a and b time series ($\bar{a_\tau}$ and $\bar{b_\tau}$, respectively) are used for each instead of the mean values from the whole time series used in the DCF method. However, our sparse data (one data point extracted from a separate orbit which is about 10 times shorter compared to the intervals between the orbits) do not allow us to use the LCCF technique along with a Monte Carlo method to estimate the significance of cross-correlations between the time series presented in Max-Moerbeck et al. (2014). Therefore, the aforementioned soft lag cannot be considered as statistically significant.

On the daily time-scales, we do not observe a significant delay between the 0.3–2 keV and 2–10 keV fluxes for the well-sampled flare observed in Period 1.

We have also constructed a scatter plot for the contemporaneous daily-binned 0.3–10 keV and VHE fluxes in the count s^{-1}–ph cm^{-2} s^{-1} representation since the later data are not provided in erg cm^{-2} s^{-1} units in the original papers (Fig. 7f). The absence of a correlation between these quantities cannot be simply related to the sparsely sampled data. No correlation is evident even in the case of densely sampled XRT and MAGIC observations during a week-long multi-wavelength campaign performed in Period 1 – the VHE flux was close to its historical minimum (see T08) while the source

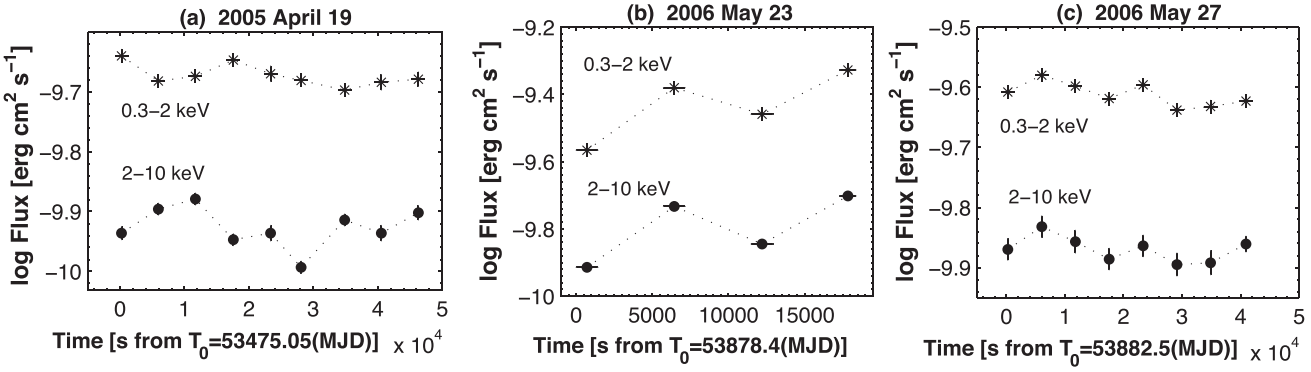

Figure 11. Cross-correlation between the soft (0.3–2 keV) and hard (2–10 keV) fluxes. The first figure shows a variability of these fluxes with time during 2005–2013, and the correlation between them is shown in the second panel of upper row. In the second row, the evolution of hard and soft fluxes with time and corresponding DCF plots is shown for the different XRT pointings (exhibiting IDVs). The solid lines represent a polynomial fit to the DCFs.

underwent an X-ray flare. Correlated flaring activities are also not seen during Periods 2, 4, 5, and 7, containing the VHE observations of the source. Fig. 7(g) also does not show a significant correlation between the contemporaneous XRT and LAT count rates binned within the 2 weeks – we did not observe increasing HE energy activity along with those in the 0.3–10 keV energy band in some periods (see Sections 3.2–3.3) and vice versa.

The 0.3–10 keV flux showed a weak correlation with those from the UVOT bands [$r = 0.30(0.11)$–$0.38(0.10)$; see Fig. 7(h) where the 0.3–10 keV and *UVW2*-band fluxes are plotted in the erg cm^{-2} s^{-1} units]. Note that the soft X-ray flux exhibited a stronger correlation with the fluxes from all UVOT bands [$r = 0.40(0.10)$–$0.52(0.09)$] while the hard flux is significantly weaker correlated with them [$r = 0.28(0.12)$–$0.35(0.11)$; see Table 9], and it does not exhibit a correlation at the 99 per cent confidence with *B*- and *V*-band fluxes. There is also no correlation between the contemporaneous daily-binned XRT and *R*-band fluxes at the 99 per cent confidence. Finally, the fluxes from different UVOT bands show a very strong correlation with each other [$r = 0.70(0.06)$–$0.78(0.05)$].

Our study of multi-wavelength cross-correlations has revealed that the one-zone synchrotron self-Compton (SSC) scenario was not always suitable for 1ES 1959+650 during the 9.5 yr period. The X-ray flares were sometimes not accompanied with an increasing activity in the γ-ray part of the spectrum and vice versa. In some cases, the radio–UV fluxes showed long-term decay trends when the source underwent an X-ray flare. Even in the epochs of a correlated behaviour of XRT and UVOT light curves, the latter often showed a delay by several days. Similar to the prominent 'orphan' TeV event in 2002, significant flares in the HE and VHE bands in Periods 4 and 7 were not accompanied by those in the synchrotron part of the spectrum.

6 DISCUSSION

6.1 Flux variability character and amplitudes

Our timing analysis of long-term *Swift*–XRT observations of 1ES 1959+650 has revealed tens of the 0.3–10 keV flux variability events from the fluctuations observed within 1 ks to the long-term flares lasting a few months. The duty cycle (DC; i.e. the fraction of total observation time during which the object displays a variability) of the IDVs detected at the 3σ confidence is 22.5 per cent and this parameter attains 28.2 per cent including the IDVs, detected at 99.5 per cent confidence. Note that this source is less variable on the intra-day time-scales than PKS 2155−304 (48 per cent; K14). The non-detection of IDVs for other pointings cannot be simply related to the shorter exposures since only about 40 per cent out of them are shorter than 1 ks, and, nevertheless, we have the detections even on these time-scales. Furthermore, the source was non-variable during some relatively long observations. For example, it did not show a flux variability in the case of the 2006 May 25 (MJD 53880.44) pointing with the 4.9 ks exposure distributed over the 46.9 ks interval (nine orbits), and during the 2009 September 26 observation (MJD 55100.69) with the 6.2 ks exposure (five orbits, $\Delta t = 24.6$ ks). Therefore, we may conclude that the source showed an unequal activity at the intra-day time-scales in different epochs. From the *ARGOS* observations, Giebels et al. (2002) concluded that the source did not appear to vary significantly at the time-scales shorter than a day, and the flux did not change more than a few per cent at the time-scales shorter than a day from the *RXTE*-PCA data. The same authors did not also reveal an indication of a 0.1–2.4 keV flux variability from the *ROSAT* pointing of 1996 April 1 which lasted for a total of half a day. Furthermore, our study of X-ray IDVs shows that they mostly occurred in higher brightness states – the mean value of corresponding count rates is 8.06 count s^{-1}, and only six out of total 26 events are observed in the epochs when the source showed the count rates below the mean level for the 2005–2014 period (see Section 3.1). The pointings with $F_{0.3-10\,\mathrm{keV}} \lesssim 5$ count s^{-1} mostly show the variability detection below the 1σ significance. Note that the intra-day X-ray variability in PKS 2155−304 did not reveal a correlation with the brightness state and a very fast event was recorded when the source exhibited its one of the lowest flux levels (see K14). It is therefore easier to explain the intra-day activity of 1ES 1959+650 in the framework of shock-in-jet scenario (interaction of a propagating shock front with the jet inhomogeneities; Sokolov, Marscher & McHardy 2004) rather than via other instability mechanisms, e.g. those occurring near the event horizon of central black hole which should be more conspicuous when the source is faint (see e. g. Mangalam & Wiita 1993; Kapanadze 2009). In that case, the variable emission from the black hole vicinity will not be 'shadowed' by the huge amount of the flux generated by the emission zone following the shock front which propagates towards the observer.

From the previous studies, the fastest X-ray events were reported by Krawczynski et al. (2004) – a flux increase and decay with the e-folding time of 5.9 h and 15.2 h, respectively, from the *RXTE*-PCA observations of 2002 May–June. Furthermore, the presence of VHE IDVs was reported by Holder et al. (2003) during the prominent 'orphan' TeV flare of 2002 (a flux doubling in 7 h) and a variability on the 3 ks time-scale is detected in our study from the VERITAS data of 2012 May, presented by Aliu et al. (2014). We therefore conclude that the X-ray–γ-ray photons are sometimes produced within the very compact area of 1ES 1959+650.

Similar to our target, very fast X-ray variability occurring on the time-scales less than 1 ks has been reported for PKS 2155−304 (a successive increase and drop of the 0.3–10 keV flux within 0.7 ks; K14) and Mrk 501 (an increase of the 2–10 keV flux by 60 per cent in 200 s, followed by a drop by 40 per cent in 600 s; Catanese & Sambruna 2000). However, the latter detection was attributed to the instrumental effects by Xue & Cui (2005).

The source did not show periodical variations. It is clear that 1ES 1959+650 varied significantly slowly in the optical bands – the well-sampled historical *R*-band light curve shows the long-term flares lasting from several months to more than one year. It is not therefore a surprise that no optical IDVs at 3σ confidence was found for this source during 21 nights in the *B, V, R, I* bands by Gaur et al. (2012) and during 35 nights in *R* band by Kapanadze (2013).

According to Saito et al. (2013), the flux doubling time can also serve for constraining the upper limit to the emission region as

$$R_{\mathrm{em}} \leqslant \frac{c\tau_{\mathrm{d}}\Gamma_{\mathrm{em}}}{1+z}. \quad (17)$$

Adopting the value $\Gamma_{\mathrm{em}} = 40$ from Aliu et al. (2014) used for the fast VHE flare on MJD 56067 with $\tau_{\mathrm{d}} = 1.47$ ks (see Section 3.5), we obtain $R_{\mathrm{em}} \leq 1.7 \times 10^{15}$ cm.

The fractional variability amplitudes of the IDVs show an anti-correlation with the 0.3–10 keV flux. The highest value $F_{\mathrm{var}} = 19.31 \pm 2.72$ per cent was derived from the observation with $F_{0.3-10\,\mathrm{keV}} = 2.88 \pm 0.07$ count s^{-1} while the smallest variability amplitudes correspond to the pointings performed in Period 1 when the source, on average, exhibited its highest historical X-ray flux compared to those from other periods. Note that an anti-correlation between

fractional amplitude and flux was also reported by Zhang et al. (2006) that was suggested to be as indication of a strong non-stationary origin of the X-ray variability.

The source shows an increasing variability power towards longer time-scales – while $F_{\rm var} < 20$ per cent for IDVs, it was generally higher for relatively well-sampled long-term flares, and it reached about 98 per cent on one occasion. This property, referred to as 'red noise' (see Aleksic et al. 2015), is one of the well-known properties for blazars. Using the power spectral density (PSD) technique for well-sampled long-term light curves, different authors showed the presence of larger variability at smaller frequencies/longer time-scales in the form $P_\nu \propto \nu^{-\alpha}$ with spectral index α between 1 and 2 (see Uttley, McHardy & Papadakis 2002; Chatterjee et al. 2008, 2012; Abdo et al. 2010; Aleksic et al. 2015, etc.). For the 2009 multi-wavelength campaign on Mrk 421, Aleksic et al. (2015) derived the range $\alpha = 1.3$–2.0 from the VHE frequencies towards the OVRO 15 GHz. However, our much sparsely sampled data did not allow us to perform the PSRESP simulations (Uttley et al. 2002, and references therein) for 1ES 1959+650 to construct the intrinsic PSD of its XRT, UVOT and VHE light curves, and study its properties.

6.2 Spectral variability

A trend for increasing fractional variability amplitude with the frequency in 1ES 1959+650 is an indication of a strong spectral variability in the 0.3–10 keV flux. This result has been confirmed by our detailed spectral analysis. Namely, the source showed a broad range of the photon index at 1 keV $a = 1.76$–2.39 which is broader compared to that reported by M08 from the *BeppoSAX*, *XMM–Newton* and *Swift*–XRT observations of this source. However, the broader ranges of this parameter have been reported for Mrk 421 ($a = 1.61$–2.54), Mrk 501 (1.41–2.22), PKS 0548−322 (1.53–2.40) (M04; M08; T07; T09). On average, our target is significantly harder than PKS 2155−305 ($a = 2.04$–2.79) with a distribution peak at $a = 2.45$ (K14) versus $a_{\rm peak} = 2.01$ for 1ES 1959+650. This is also evident from the distribution of the HR quantity – it shows a range of 0.317–0.918 for the later source while the range of 0.145–0.543 was reported by K14 for PKS 2155−304. Note that even higher values of the HR with $HR_{\rm max} = 0.99$ were presented by Giebels et al. (2002) for our target.

Our study has revealed that a showed a variability both during the long-term and day-to-day flux changes and in the case of some IDVs. The spectral changes mainly followed a 'harder-when-brighter' evolution with pure or dominantly CW loops in a HR-flux plane. The episodic changes to an opposite evolution were mainly related to the emergence of a short-term outburst, superimposed on a longer-trend variability. A similar spectral behaviour was evident also for PKS 2155−304, although a flare with a pure CCW spectral evolution was also reported for this source by K14. From the previous studies, Giebels et al. (2002) reported a spectral variability with $\Delta\Gamma = 0.3$ in the 2–16 keV range and the spectrum was harder when the source got brighter. A similar spectral evolution was also reported by Krawczynski et al. (2004) from the PCA 2002 May–June observations.

As reported in Section 4, the X-ray spectra of 1ES 1959+650 are generally curved. They were fitted well with the LP model with a broad range of the curvature parameter ($b = 0.14$–0.67). Although M08 also reported a wide range of this parameter from the *Swift*–XRT observations from the 2005–2006 period, the value $b = 0.75 \pm 0.03$ from Obs ID 00035025010 is significantly higher compared to the range of the b parameter obtained by us from the orbit-resolved spectral analysis (see Table 6), and the mean of these values is close to $b = 0.33 \pm 0.05$ provided for the same observation in Tagliaferri et al. (2008). Probably, the aforementioned high spectral curvature reported by M08 is related to the use of common source extraction region for all orbits of this observation. The range of b parameter for 1ES 1959+650 is significantly wider compared to that reported for Mrk 421 (0.07–0.48), Mrk 501 (0.12–0.33), PKS 0548−322 (0.22–0.56), H 1426+428 (0.12–0.49) (see M04; M08; T07; T09). A similar broad range of this parameter ($\Delta b = 0.67$ with the distribution peak at $b = 0.37$) was reported for PKS 2155−304 in K14.

According to M04, a curved spectral distribution of the particles with energy develops when the acceleration probability is a decreasing function of the electron energy (so-called energy-dependent acceleration probability process, EDAP). In this scenario, a linear relation between a and b is expected. However, we have found no significant positive correlation between them either for the total 2005–2014 period or for individual flares, in contrast to the *BeppoSAX* observations of Mrk 421 during 1997–1999 period where a strong correlation between these parameters was evident (M04). In the framework of the same scenario, an anti-correlation between the b and $E_{\rm p}$ parameters is expected (Tramacere, Massaro & Cavaliere 2007). Namely, both parameters are related to the fractional acceleration gain ε as $E_{\rm p} \propto \varepsilon$ and $r \propto (\log \varepsilon)^{-1}$ with $b \approx r/5$, respectively. However, our spectral analysis did not reveal a significant correlation between these parameters for 1ES 1959+650 (as for the whole 2005–2014 period, as for the individual long-term flares and intra-day events) in contrast to the *ASCA*, *BeppoSAX*, *XMM–Newton* observations of Mrk 421 performed during 1997–2005 (T09).

On the other hand, a curved spectral distribution can be established via the stochastic acceleration which arises from the magnetic turbulence close to the shock front (T09). Massaro, Paggi & Cavaliere (2011) showed that the electrons in the jets of TeV detected HBLs (so-called TBLs, including 1ES 1959+650) should undergo a more efficient stochastic acceleration than in those of the TeV-undetected HBLs (UBLs). The same authors showed that the synchrotron SEDs are relatively broader (i.e. the curvature is smaller with $b \backsimeq 0.3$) when the stochastic acceleration is more efficient while they are narrower ($b \backsimeq 0.7$) in the opposite case. Our study of the curvature parameter from the XRT spectra of 1ES 1959+650 shows its distribution maximum at $b = 0.35$, i.e. the source mainly exhibited broader synchrotron SEDs expected when the stochastic mechanism is more efficient. Furthermore, our detection of an anti-correlation between b and the 0.3–10 keV flux shows a trend of lower curvatures with higher fluxes (i.e. lower curvatures in flaring states) while the higher curvatures are observed mainly during the lower brightness states (see Section 4 for details). This result also favours a stochastic acceleration of the electrons producing X-ray photons during the flares. However, the weakness of the b–$F_{0.3-10\,\rm keV}$ correlation and the examples of an increase of spectral curvature with the flux, provided in Section 4, can be related to a 'contamination' of a stochastic acceleration of the electrons by the cooling processes (A. Tramacere, private communication).

Similar to EDAP, an anti-correlation between the b and $E_{\rm p}$ parameters is also expected in the framework of the stochastic acceleration scenario when a mono-energetic or quasi-mono-energetic particle injection in the acceleration zone occurs (T09). However, the absence of this correlation leads to the suggestion that the assumption about the mono-energetic/quasi-mono-energetic injection is not true for our target, and a more complex particle injection scenario is necessary for the stochastically accelerated electrons, responsible for the production of X-ray photons during the flares.

The LP model gives a wide range of the E_p parameter for the 0.3–10 keV spectra, varying from 0.12 to 1.84 keV. In fact, the range of this parameter can be larger since those values with $E_p \lesssim 0.8$ keV should be considered as upper limits to the intrinsic ones. As for the poor spectra, fitted better with the simple power law, we derived the SED peak location with equations (8) or (9) which give the E_p values within the aforementioned interval. This range is wider than that reported by M08 ($E_p = 0.76$–1.74 keV). Thus, 1ES 1959+650 has been always found to be a soft X-ray peaked BLL. Nevertheless, Tagliaferri et al. (2003) reported the synchrotron peak to be located in the 0.1–0.7 keV range based on the *BeppoSAX* 2001 September observations. The soft X-ray values of the E_p parameter were reported also for Mrk 421 (0.12–0.78 keV), PG 1553+113 (0.40–0.61 keV), H 1426+428 (0.80–2.00 keV) in T07 and M08 from the XRT observations. The synchrotron SED peaks are found in the far-UV–soft X-ray part of the spectrum in the case of PKS 2155−304 ($E_p < 0.89$ keV) by K14. The peaks at hard X-rays were reported for PKS 0548−322 (2.10–4.13 keV; M08), and Mrk 421 from the *BeppoSAX* pointings performed in 2000 (2.10–5.50 keV; M04). To date, the widest range of the E_p parameter from 0.94 keV (M08) to beyond 50 keV (Pian et al. 1998, in the epoch of a dramatic flare of 1997 April) has been reported for Mrk 501.

During some flares, E_p moved towards higher energies and to the opposite direction – during the flux decay phase while no clear trend was seen in many cases. Different flaring events showed a shift of the synchrotron peak with $\Delta E_p = 0.34$–0.92 keV. The most extreme variability was observed during the 2009 July–September event when the SED peak moved by 0.92 keV to the maximum value $E_p = 1.34$ keV, and then showed $\Delta E_p = -0.84$ keV with the flux decay. This parameter exhibited a large variability on the daily and intra-day time-scales with maximum increase of 0.75 keV in 0.8 d and decay by 0.77 keV in 0.5 d. From the previous studies of this source, a move of synchrotron peak to higher energies with increasing fluxes was reported by Tagliaferri et al. (2003). Among other HBLs, an extreme behaviour of increase and decay by a few keV with the 0.3–10 keV flux within a single *Swift*–XRT observations of Mrk 421, performed in 2006, was reported by T09. However, the most extreme shift by a factor of $\gtrsim 100$ to hard X-rays was observed for Mrk 501 during the aforementioned flare.

According to M08, the detection of the correlation $S_p(L_p) \propto E_p^{\alpha}$ may be used to draw a conclusion about the physical factor (variations of the electron average energy/magnetic field/beaming factor/number of emitting particles) which makes the main contribution in the observed spectral variability of the source (depending on the values of the α parameter). The *Swift*–XRT observations of 2013–2014 yield $\alpha = r_{\log}(S_p, E_p) = 0.24 \pm 0.11$ for 1ES 1959+650. Note that this value is significantly lower compared to $\alpha = 1$ when the spectral changes are dominated only by variations in the average energy and number of the emitting electrons is constant (even higher values of this parameter are expected for other dominant physical factor; see e.g. T09). This result shows that the spectral variability in 1ES 1959+650 is complex and it cannot be defined by a single factor. On the other hand, the aforementioned relation is obtained in the framework of the synchrotron emission mechanism from one dominant homogenous component that may not be an appropriate assumption for our target. M08 revealed a stronger correlation between the L_p and E_p quantities for the TBLs PKS 0548−322, Mrk 421, 1H 1426+428, Mrk 501 with $r_{\log} = 0.61$–0.89 from the *BeppoSAX*, *XMM–Newton* and *Swift*–XRT observations performed during 1996–2007.

6.3 Inter-band cross-correlations

The lack of correlation between the X-ray and γ-ray emissions seems to be intrinsic for 1ES 1959+650. In addition to the 'orphan' flare of 2002 June, the VHE and HE flares at the end of 2009 May and 2012 May were not accompanied with an increasing activity in the radio–X-ray parts of the spectrum (see Section 3.2). A VHE flash occurred during the days when the 0.3–10 keV flux showed a dip. A similar behaviour was observed in Period 7 when the strong VHE outburst (accompanied by a relatively moderate flux increase in the LAT band) coincided with an X-ray dip during those days, and no increasing activities in the radio–UV bands were recorded. On the other hand, an X-ray flare was not accompanied with those in the VHE and HE bands in Period 1, Period 2, 2010 May–June and September flares. A similar result was reported by Blazejowski et al. (2005) for Mrk 421 when a very fast X-ray flare, lasting only ∼20 min, was recorded and no higher-energy counterpart was detected. For our target, a strong X-ray variability was not accompanied by a flaring behaviour in the VHE band during the 2003 multi-wavelength observations (Gutierrez et al. 2006). Note that in the middle of Period 7, when the source exhibited an X-ray flare, other bands of the synchrotron spectrum showed a long-term decay (see Section 3.3). We suggest that this flare may be produced by a separate population of accelerated electrons. A similar case was reported for PKS 2155−304 in K14. Furthermore, for some epochs when the source exhibited a flaring behaviour in all spectral bands, the optical–UV light curves showed a delay by 2–9 d with respect to that from the 0.3–10 keV band. These events, in combination with an uncorrelated behaviour in Period 7, yielded a relatively weak correlation between the XRT and UVOT bands during the 2005–2014 period.

7 CONCLUSIONS

We have presented the results of long-term *Swift*–XRT observations of the HBL source 1ES 1959+650 during 2005–2014. It exhibited a strong long-term variability of the 0.3–10 keV flux with the maximum-to-minimum ratio of about 8. The flux variability showed an erratic character changing its amplitude and minimum flux level from flare to flare. The fractional variability amplitude showed an increasing trend towards higher frequencies as $F_{\rm var}(E) \propto E^m$ with different values of the m parameter in different periods. For this source, the 19 cases of intra-day flux changes with fractional rms variability amplitudes of 3.2–19.1 per cent are revealed, observed mainly at the higher brightness states. They sometimes occurred on the time-scales as short as ∼1 ks. The X-ray flares were sometimes not accompanied with an increasing activity in the γ-ray part of the spectrum and vice versa. In some cases, the radio–UV fluxes showed a long-term decay trends when the source underwent an X-ray flare. Similar to the prominent 'orphan' TeV event in 2002, significant flares in the HE and VHE bands in 2009 May and 2012 May were not accompanied by those in the synchrotron part of the spectrum. This uncorrelated behaviour can be explained by the existence of different populations of accelerated electrons, responsible for the emissions in the different parts of the spectrum.

The flaring activity in different epochs was accompanied by a significant spectral variability. The X-ray spectra were generally curved, and, therefore, fitted well with the LP model. They showed wide ranges of photon index at 1 keV ($\Delta a = 0.63$), location of SED peak ($\Delta E_p > 1.72$ keV), and curvature parameter ($\Delta b = 0.53$). Our study has significantly expanded the ranges of these

parameters compared to those obtained within previous studies for the restricted time intervals. The photon index at 1 keV varied both at the weekly–monthly and on the intra-day time-scales, and the source showed mainly a 'harder-when-brighter' spectral evolution. The synchrotron SED location mainly shifted towards higher energies with a flux increase, and vice versa. In contrast, the curvature parameter showed an anti-correlation with the 0.3–10 keV flux during the major parts of different flares. The lack of a correlation between photon index and curvature, predicted by the EDAP scenario, leads to the suggestion that this mechanism is less relevant for the acceleration of the electrons responsible for X-ray flares. We concluded that the stochastic acceleration of the electrons from the magnetic turbulence close to the shock front may be more important for our target since it showed mainly lower curvatures (i.e. broader synchrotron SEDs) during the X-ray flares expected when the stochastic mechanism is more efficient. However, the stochastic acceleration should be contaminated by other type of acceleration mechanisms and cooling processes in some cases. The bolometric synchrotron luminosity ranged between 5.8×10^{44} erg s^{-1} and 5.46×10^{45} erg s^{-1} during the 9.5 yr period.

Our study of a long-term behaviour of 1ES 1959+650 shows that the source was highly variable in the X-ray as well in the optical, UV and γ-ray bands, accompanied with a significant spectral variability that exhibited a complex and, sometimes, an unpredictable character. Further, more densely sampled multi-wavelength observations are necessary for a deeper study of non-stationary processes responsible for these variations, and establish the ranges of inter-band lags.

ACKNOWLEDGEMENTS

BK thanks Andrea Tramacere, Enrico Massaro, Paolo Giommi, Dave Davis and Tyrel Johnson for useful suggestions. BK, SK and TM acknowledge the Shota Rustaveli National Science Foundation grant FR/377/6-290/14. PR acknowledges the contract ASI-INAF I/004/11/0. BK thanks the *Swift* PI, Neil Gehrels, for approving his requests for the ToO observations. We acknowledge the helpful service of HEASARC, and the use of public data from the *Swift* and *Fermi* archives. This research has made use of the XRTDAS software, developed under the supervision of the ASDC, Italy, and the data from the OVRO 40-m monitoring programme which is supported in part by NASA grants NNX08AW31G and NNX11A043G, and NSF grants AST-0808050 and AST-1109911. This research has made use of the *Swift*–BAT 70-Month Hard X-ray Survey data and the quick-look results, provided by the *RXTE*-ASM team. Finally, we thank the anonymous referee for his/her very useful comments and suggestions that helped us to improve the quality of the paper.

REFERENCES

Abdo A. A. et al., 2009, ApJ, 707, 1310
Abdo A. A. et al., 2010, ApJ, 722, 520
Abramowski A. et al., 2010, A&A, 520, 83
Acero F. et al., 2015, ApJS, 218, 23
Albert J. et al., 2006, ApJ, 639, 761
Aleksic E. et al., 2015, A&A, 576, 126
Aliu E. et al., 2013, ApJ, 775, 3
Aliu E. et al., 2014, ApJ, 797, 89
Andruchow I., Romero G. E., Cellone S. A., 2005, A&A, 442, 57
Backes M., 2011, PhD thesis, Technical Univ. Bokhum
Barthelmy S. D. et al., 2005, Space Sci. Rev., 120, 143
Baumgartner W. H., Tueller J., Markwardt C. B., Skinner G. K., Barthelmy S., Mushotzky R. F., Evans P. A., Gehrels N., 2013, ApJS, 207, 19
Beckmann V, Wolter A., Celotti A., Costamante L., Ghisellini G., Maccacaro T., Tagliaferri G., 2002, A&A, 383, 410
Blazejowski M. et al., 2005, ApJ, 630, 130
Breeveld A. A., Landsman W., Holland S. T., Roming P., Kuin N. P. M., Page M. J., 2011, AIP Conf. Ser. Vol. 1358. An Updated Ultraviolet Calibration for the Swift/UVOT. Am. Inst. Phys., New York, p. 373
Burrows D. N. et al., 2005, Space Sci. Rev., 120, 165
Catanese. M., Sambruna R., 2000, ApJ, 534, L39
Celotti A., Ghisellini G., 2008, MNRAS, 385, 283
Chatterjee R. et al., 2008, ApJ, 689, 79
Chatterjee R. et al., 2010, ApJ, 749, 191
Chiappetti L. et al., 1999, ApJ, 521, 552
Comastri A., Molendi S. E., Ghisellini G., 1995, MNRAS, 277, 297
Edelson R. A., Krolik J. H., 1988, ApJ, 333, 646
Elvis M., Plummer D., Schachter J., Fabiano G., 1992, ApJS, 80, 257
Fitzpartick E. L., Messa D., 2007, ApJ, 663, 320
Furniss A. K., 2013, PhD thesis Univ. California
Gaur H. et al., 2012, MNRAS, 420, 3147
Gehrels N. et al., 2004, ApJ, 611, 1005
Giacconi R. et al., 1979, ApJ, 230, 540
Giebels B. et al., 2002, ApJ, 571, 763
Gutierrez K. et al., 2006, ApJ, 644, 742
Güver T., Özel F., MNRAS, 400, 2050
Holder J. et al., 2003, ApJ, 583, L9
Kalberla P. M. W., Burton W. B., Hartmann D., Arnal E. M., Bajaja E., Morras R., Pppel W. G. L., 2005, A&A, 440, 775
Kapanadze B. Z., 2009, MNRAS, 398, 832
Kapanadze B., 2013, AJ, 145, 31
Kapanadze B., Janiashvili E., 2012, Ap&SS, 339, 339
Kapanadze B., Romano P., Vercellone S., Kapanadze S., 2014, MNRAS, 444, 1077 (K14)
Kesteven M. J. L., Bridle A. H., Brandie G. W., 1976, AJ, 81, 11
Krawczynski H. et al., 2004, ApJ, 601, 151
Krim H. et al., 2013, ApJ, 209, 14
Landau R. et al., 1986, ApJ, 308, 78
Mangalam A. V., Wiita P. J., 1993, ApJ, 406, 420
Massaro E., Perri M., Giommi P., Nesci R., 2004, A&A, 413, 489 (M04)
Massaro F., Tramacere A., Cavaliere A., Perri M., Giommi P., 2008, A&A, 478, 395
Massaro F., Paggi A., Cavaliere A., 2011, ApJ, 742, L32
Max-Moerbeck W., Richards J. L., Hovatta T., Pavlidou V., Pearson T. J., Readhead A. C. S, 2014, MNRAS, 445, 437
Moretti A. et al., 2005, UV, X-ray, and Gamma-Ray Space Instrumentation for Astronomy XIV. Proc. SPIE Vol. 5898, p. 360
Nishiyama T., 1999, in Kieda D., Salamon M., Dingus B., eds, Proc. 26th Int. Cosmic Ray Conf., Vol. 3, Under the auspices of the International Union of Pure and Applied Physics (IUPAP). p. 370
Padovani P., Giommi P., 1995, ApJ, 444, 567
Perlman E. S. et al., 1996, ApJS, 104, 251
Perlman E. S. et al., 2005, ApJ, 625, 727
Pian E. et al., 1998, ApJ, 492, L17
Poole T. S., 2008, MNRAS, 383, 627
Richards J. L. et al., 2011, ApJS, 194, 209
Romano P. et al., 2006, A&A, 456, 917
Roming P. W. A. et al., 2005, Space Sci. Rev., 120, 95
Saito S., Stawarz L., Tanaka Y. T., Takahashi T., Madejski G., D'Ammando F., 2013, ApJ, 766, L11
Scarpa R., Urry C. M., Falomo R., Pesce J. S., Treves A., 2000, ApJ, 532, 740
Schachter J. F. E. et al., 1993, ApJ, 412, 541
Sorcia M. et al., 2013, ApJS, 206, 11
Sokolov A., Marscher A. P., McHardy I. M., 2004, ApJ, 613, 725
Tagliaferri G., Ravasio M., Ghisellini G., Tavecchio F., Giommi P., Massaro E., Nesci R., Tosti G., 2003, A&A, 412, 711
Tagliaferri G. et al., 2008, ApJ, 679, 1029

Tramacere A., Massaro F., Cavaliere A., 2007, A&A, 466, 521
Tramacere A., Giommi P., Perri M., Verrecchia F., Tosti G., 2009, A&A, 501, 879 (T09)
Uellenbeck M., 2013, PhD thesis, Technical Univ. Bokhum
Uttley P., McHardy I. M., Papadakis I. E., 2002, MNRAS, 332, 231
Vaughan S., Edelson R., Warwick R. S., Uttley P., 2003, MNRAS, 345, 1271
Vaughan S. et al., 2006, ApJ, 638, 904
Vercellone S. et al., 2010, ApJ, 712, 405
Wagner S., Witzel R., 1995, ARA&A, 33, 163
Xue Y., Cui W., 2005, ApJ, 622, 160
Zhang Y. H., 2008, ApJ, 682, 789
Zhang Y. H. et al., 2002, ApJ, 572, 762
Zhang Y. H., Treves A., Celotti A., Qin Y. P., Bai J. M., 2005, ApJ, 629, 686
Zhang Y. H., Treves A., Maraschi L., Bai J. M., Liu F. K., 2006, ApJ, 637, 699

SUPPORTING INFORMATION

Additional Supporting Information may be found in the online version of this article:

Table 1. The summary of the *Swift*–XRT observations.
Table 2. The results of the *Swift*–UVOT observations.
Table 5. The summary of IDVs at the 99.9 and 99.5 per cent confidences from the *Swift*–XRT observations of 1ES 1959+650.
Table 6. The summary of the XRT spectral analysis with log-parabolic model.
Table 9. Correlations between different spectral parameters and multi-band fluxes.
Figure 4. Light curves from the observations with IDVs at the 99.9 per cent confidence (extract).
Figure 5. Light curves from the observations with IDVs at the 99.5 per cent confidence (extract).
Figure 7. Correlation between different spectral parameters and fluxes (extract).
Figure 8. 0.3–10 keV fluxes, curvature parameter and E_p plotted versus time for different long-term flares and IDVs (extract).
Figure 9. HR – 0.3–10 keV flux planes corresponding to different long-term X-ray flares and IDVs (extract).
(http://mnras.oxfordjournals.org/lookup/suppl/doi:10.1093/mnras/stv3004/-/DC1)

Please note: Oxford University Press is not responsible for the content or functionality of any supporting materials supplied by the authors. Any queries (other than missing material) should be directed to the corresponding author for the article.

This paper has been typeset from a TEX/LATEX file prepared by the author.